

*Digital Comprehensive Summaries of Uppsala Dissertations  
from the Faculty of Science and Technology 2636*

# The Role of Kinetic Waves in the Solar Wind Evolution

JOAN JORDI BOLDÚ-O' FARRILL TREVIÑO



ACTA UNIVERSITATIS  
UPSALIENSIS  
2026

ISSN 1651-6214  
ISBN 978-91-513-2734-1  
urn:nbn:se:uu:diva-578455



UPPSALA  
UNIVERSITET

Dissertation presented at Uppsala University to be publicly examined in Sonja Lyttkens (101121), Ångströmlaboratoriet, Regementsvägen 10, Uppsala, Tuesday, 24 March 2026 at 09:00 for the degree of Doctor of Philosophy. The examination will be conducted in English. Faculty examiner: Professor Xóchitl Blanco-Cano (Universidad Autónoma de México (UNAM)).

### **Abstract**

Boldú-O' Farrill Treviño, J. J. 2026. The Role of Kinetic Waves in the Solar Wind Evolution. *Digital Comprehensive Summaries of Uppsala Dissertations from the Faculty of Science and Technology* 2636. 74 pp. Uppsala: Acta Universitatis Upsaliensis. ISBN 978-91-513-2734-1.

The solar wind is a continuous and turbulent stream of charged particles and magnetic field originating from the solar corona. As it expands it fills the solar system and creates the heliosphere. The global dynamics of the heliosphere are typically described by magnetohydrodynamic (MHD) models. However, many of the observed properties of the solar wind, such as temperature and bulk velocity, cannot be entirely described within the MHD framework. In the low-density, high-temperature environment of the solar wind, particle collisions are infrequent. Consequently, the solar wind is a weakly collisional plasma that readily deviates from local thermodynamic equilibrium (LTE)-a characteristic not accounted for by ideal MHD models. These non-equilibrium conditions manifest as non-Maxwellian features in the ion and electron velocity distribution functions (VDFs).

However, deviations from LTE are constrained by plasma instabilities, which prevent the indefinite growth of non-Maxwellian features, such as beam components or temperature anisotropies. By exciting electrostatic and electromagnetic waves, these instabilities redistribute energy and drive the plasma toward more stable configurations. Because these processes occur at scales where MHD equations are no longer valid, a kinetic theory is required. This thesis investigates the role of kinetic waves arising from unstable VDF configurations using data from the Solar Orbiter mission. By probing the inner heliosphere at heliocentric distances between 0.28 and 1.1 au, Solar Orbiter provides continuous measurements that allow for the study of the radial evolution of solar wind properties.

We identify and characterize several kinetic wave modes critical to solar wind evolution, establishing their occurrence rates and dependence on heliocentric distance. We further associate these waves with transient solar wind phenomena that facilitate their emission, such as magnetic holes, interplanetary (IP) shocks, and radio burst source regions. Our results show that Langmuir waves are preferentially excited within localized magnetic field depressions, while ion-acoustic wave activity is significantly enhanced in the vicinity of IP shocks. Furthermore, a detailed analysis of an individual IP shock links its macroscopic structure to the kinetic behavior of ions, which is, in turn coupled to electron-scale processes through the excitation of ion-acoustic waves. In general, these results demonstrate that kinetic waves are a recurring feature of the solar wind, typically associated with larger-scale structures where the development of unstable VDF configurations readily occurs. This cross-scale coupling reflects the necessity of studying the solar wind across multiple scales, and in particular kinetic scales, to fully understand its evolution.

Finally, we refine existing electron density calibration methods based on Solar Orbiter spacecraft potential measurements. This refinement enables the retrieval of electron density at the high temporal resolution necessary to investigate kinetic-scale processes in the solar wind.

*Keywords:* Solar wind, space plasma physics, plasma waves

*Joan Jordi Boldú-O' Farrill Treviño, Department of Physics and Astronomy, Box 516, Uppsala University, SE-751 20 Uppsala, Sweden.*

© Joan Jordi Boldú-O' Farrill Treviño 2026

ISSN 1651-6214

ISBN 978-91-513-2734-1

URN urn:nbn:se:uu:diva-578455 (<http://urn.kb.se/resolve?urn=urn:nbn:se:uu:diva-578455>)

*Para Göran, Linnéa, Agnes y Poppi*



# List of papers

This thesis is based on the following papers, which are referred to in the text by their Roman numerals.

- I *Langmuir Waves Associated with Magnetic Holes in the Solar Wind*  
**J. J. Boldú**, D. B. Graham, M. Morooka, M. André, Yu. V. Khotyaintsev, T. Karlsson, J. Souček, D. Píša and M. Maksimovic.  
*Astronomy and Astrophysics* (2023). Volume 674, Solar Orbiter First Results (Nominal Mission Phase) doi: 10.1051/0004-6361/202346100.
  
- II *Ion-acoustic Waves Associated with Interplanetary Shocks*  
**J. J. Boldú**, D. B. Graham, M. Morooka, M. André, Yu. V. Khotyaintsev, A. Dimmock, D. Píša, J. Souček, M. Maksimovic, P. Louarn, A. Fedorov, G. Nicolaou, and C. Owen.  
*Geophysical Research Letters* (2024),51,e2024GL109956. doi: 10.1029/2024GL109956
  
- III *Kinetic Structure of an Interplanetary Shock Observed at Two Heliocentric Longitudes*  
**J.J. Boldú** , D. B. Graham, M. Morooka , M. André, Yu. V. Khotyaintsev, A. Dimmock, A. Lalti, D. Píša, J. Souček, M. Maksimovic, P. Louarn, A. Fedorov, and C. J. Owen.  
Under review in *Journal of Geophysical Research: Space Physics*.
  
- IV *Electron Density Estimation from Spacecraft Potential Measurements using Solar Orbiter*  
**J.J. Boldú**, D. B. Graham, Yu. V. Khotyaintsev, M. Morooka, A. Eriksson, M. André, M. Maksimovic, A. Vecchio, G. Nicolaou, S. Štverák, C. J. Owen, and C. Watson.  
Submitted to *Astronomy and Astrophysics*.

Reprints were made with permission from the publishers.

This PhD thesis is partly based on the licentiate dissertation *Probing the Solar Wind Evolution with Kinetic Waves* by the same author, Uppsala University, 2023. Chapters 3 and 4 have been edited and updated. The remaining Chapters are new.

Generative AI has been employed for editorial suggestions in the writing process of this thesis and stylistic corrections to the cover image.

# List of papers not included in this thesis

- 1 *Extent of the Magnetotail of Venus From the Solar Orbiter, Parker Solar Probe and BepiColombo Flybys*  
N. J. T. Edberg, D. J. Andrews, **J. J. Boldú**, A. P. Dimmock, Yu. V. Khotyaintsev, K. Kim, M. Persson, Uli Auster, D. Constantinescu, D. Heyner, J. Mieth, I. Richter, S. M. Curry, L. Z. Hadid, D. Píša, L. Sorriso-Valvo, M. Lester, B. Sánchez-Cano, K. Stergiopoulou, N. Romanelli, D. Fischer, D. Schmid, M. Volwerk.  
Journal of Geophysical Research: Space Physics (2024). doi: 10.1029/2024JA032603.
- 2 *Ion Dynamics Across a Low Mach Number Bow Shock.*  
D. B. Graham, Y. V. Khotyaintsev, A. P. Dimmock, A. Lalti, **J. J. Boldú**, S. F. Tigik, and S. A. Fuselier.  
Journal of Geophysical Research: Space Physics (2024), 129, e2023JA032296. doi: 10.1029/2023JA032296
- 3 *Electron Temperatures in the Ionosphere of Venus from Solar Orbiter/Radio and Plasma Waves Instrument*  
A. Vecchio, M. Maksimovic, M. I. F. Galand, X. Bonnin, P.-L. Astier, N. J. T. Edberg, D. Píša, **J. J. Boldú**, L. Matteini, T. Chust, L. Z. Hadid, M. Kretzschmar, Yu. V. Khotyaintsev, J. Souček, T. Horbury, and S. D. Bale.  
Under Review in Astronomy and Astrophysics.
- 4 *Solar Orbiter in Venus' Ionosphere: Observations from the 4th Flyby*  
N. J. T. Edberg, **J. J. Boldú**, A. I. Eriksson, K. Kim, M. Persson, D. J. Andrews, Yu. V. Khotyaintsev, A. Vecchio, M. Maksimovic, T. Chust, L. Z. Hadid, T. S. Horbury, M. I. F. Galand, L. Matteini, D. Píša, J. Souček, M. Kretzschmar, S. D. Bale.  
Under Review in Journal of Geophysical Research: Space Physics.
- 5 *On the magnetic Structure of an Unusually High Mach Number Interplanetary Shock*  
A. P. Dimmock, **J. J. Boldú**, D. Trotta, A. Lalti, M. Lindberg, H. Hietala, Yu. V. Khotyaintsev, D. B. Graham.  
Under Review in Journal of Geophysical Research: Space Physics.

# Contents

1	Introduction .....	9
2	Solar Wind .....	11
2.1	Magnetohydrodynamics .....	11
2.1.1	Fast and Slow Solar Wind .....	14
2.1.2	Parker Spiral and Solar Cycle .....	15
2.1.3	Limitations of the MHD description of the solar wind ..	18
2.2	Kinetic Theory .....	21
2.2.1	Ion-scale Kinetics .....	26
2.2.2	Electron-scale Kinetics .....	31
3	Kinetic Waves .....	34
3.1	Langmuir Waves .....	37
3.2	Ion-Acoustic Waves .....	40
3.3	Whistler Waves .....	42
4	Solar Orbiter .....	45
4.1	Radio and Plasma Waves .....	45
4.2	Solar Wind Analyzer .....	47
4.3	Magnetometer .....	47
4.4	Electron Density Estimation .....	48
5	Summary of Publications .....	52
5.1	<i>Paper I: Langmuir Waves Associated with Magnetic Holes in   the Solar Wind</i> .....	52
5.2	<i>Paper II: Ion-acoustic Waves Associated with Interplanetary   Shocks</i> .....	53
5.3	<i>Paper III: Kinetic Structure of an Interplanetary Shock   Observed at Two Heliocentric Longitudes</i> .....	54
5.4	<i>Paper IV: Electron Density Estimation from Spacecraft   Potential Measurements using Solar Orbiter</i> .....	55
6	Reflections and Outlook .....	56
7	Sammanfattning på Svenska .....	59
8	Acknowledgements .....	61
	References .....	64



# 1. Introduction

When the first spacecraft were launched into interplanetary space, it was demonstrated that space is not empty; instead, it is filled with charged particles streaming away from the Sun at supersonic velocities (Gringauz et al., 1960; Neugebauer & Snyder, 1962). While the existence of this flow was subject of intense controversy, its exciting discovery was not entirely surprising (Dessler, 1967). Physicists already predicted the existence of such a particle stream before any spacecraft could measure the conditions in interplanetary space (Chapman & Zirin, 1957). This prediction followed from careful observation of comet tails and of perturbations of the Earth's magnetic field (Eddington, 1910; Birkeland, 1914; Biermann, 1951). The origin of this particle radiation was later identified by applying a magnetohydrodynamic (MHD) model to the outermost layer of the Sun's atmosphere, the corona (Parker, 1958; Weber & Davis Jr, 1967).

The high temperatures in the corona ( $> 10^6$  K) cause electrons to be ripped from the atomic nuclei, which consist mainly of hydrogen nuclei (protons), with a small fraction of helium nuclei ( $\alpha$ -particles) and traces of heavier-element ions, such as carbon and oxygen (Ogilvie & Coplan, 1995). The resulting electrons and ions interact with each other through long-range electromagnetic forces, exhibiting a collective behavior. As a result, they form a state of matter known as a plasma, whose dynamics are governed by the electric and magnetic fields.

Describing the plasma as a fluid, Eugene Parker showed that the high temperature of the corona cannot sustain hydrostatic equilibrium, indicating that the fluid must be in hydrodynamic expansion at supersonic velocities (Parker, 1958). This expanding plasma is called the solar wind, and it fills the solar system, creating the heliosphere. The macroscopic behavior of the solar wind can be described using MHD equations, which define the plasma as a conducting fluid.

The MHD description of the solar wind is useful for describing the system at the largest scales; however, it fails to explain the details of the solar wind evolution as it travels away from the Sun, the transient phenomena that occur within it, and its interaction with planetary objects. As a single-fluid framework, MHD is unable to describe phenomena where the behavior of ions and electrons is distinct, particularly during high-frequency processes or at scales comparable to the ion gyroradius,  $\rho_i$ .

The main reason for the limitations of the classic MHD framework, is that it implies local thermodynamic equilibrium (LTE). In the solar wind, this condition is generally not satisfied because the time it takes for the plasma to expand

into the solar system is much shorter than the characteristic timescales for particle collisions to drive the system toward LTE. Therefore, a more precise description of the plasma is necessary, for example, involving kinetic plasma physics.

The kinetic description of a plasma consists of the analysis of the statistical motion of particles by defining a velocity distribution function (VDF) for each particle species. This description is useful to explain the evolution of a plasma deviating from LTE. In the solar wind, one of the main candidates to regulate the observed evolution of the VDFs, and therefore of the solar wind, are plasma waves (Marsch, 2018; Verscharen et al., 2019). Since a plasma consists of charged particles whose dynamics are governed by electromagnetic forces, it can support a wide variety of wave modes that are not present in neutral media.

This thesis aims to determine which wave modes are relevant to solar wind evolution at varying heliocentric distances and to identify the local plasma environments with which they are associated. To address these questions, we identify and characterize various wave modes that influence the evolution of the solar wind through the modification of the VDFs. We focus on electrostatic wave modes occurring in the inner solar system, defined here as the region within 1 au of the Sun (where  $1 \text{ au} \approx 1.496 \times 10^8 \text{ km}$ , the mean Sun-Earth distance). Furthermore, we investigate the role of larger-scale structures in the solar wind, such as interplanetary shocks or magnetic holes, in the generation of plasma waves at much smaller scales.

This thesis consists of a theoretical overview, three articles on kinetic waves associated with solar wind processes, and one article detailing the methodology developed to extract high-resolution electron density from spacecraft potential measurements. These electron density data are employed to analyze the role of kinetic waves in the solar wind evolution.

## 2. Solar Wind

The extreme temperatures of the solar corona produce a strong pressure-gradient force that overcomes solar gravity, accelerating plasma outward from the Sun. Since plasma consists of charged particles, it is strongly coupled to the Sun's magnetic field, which must be considered when examining the dynamics of the solar wind. In this chapter, we provide an overview of the solar wind using the MHD framework, treating plasma as a conducting fluid subject to electric and magnetic forces. We highlight the limitations of this framework, particularly at shorter scales where many mechanisms that affect the solar wind evolution occur. To address these limitations, we introduce the kinetic description of the solar wind, identifying the relevant scales at which these mechanisms operate. We define large-scale as spatial scales,  $L$ , much larger than  $\rho_i$  and the ion inertial length,  $d_i$ . In the inner solar system, these scales are often smaller than the ion collisional mean free path,  $\lambda_{mfp} \approx 3$  au (Verscharen et al., 2019). The corresponding temporal scales,  $\tau$ , are much larger than the ion gyroperiod,  $\tau_{ci}$ , but typically smaller than the ion collisional time,  $\tau_{coll}$ . Conversely, small-scales (or kinetic-scales) correspond to  $L \lesssim \rho_i, d_i$  and  $\tau \lesssim \tau_{ci}$ . It should be noted that small scales remain significantly larger than the Debye length,  $\lambda_{De}$ , ensuring that the plasma remains quasi-neutral. A detailed mathematical definition of these characteristic scales is provided in the subsequent Sections as they are introduced within their respective physical contexts. Typical values for these characteristic scales and other solar wind parameters in the inner solar system are presented in Table 2.1; however, it should be noted that the solar wind is a highly turbulent medium characterized by significant and frequent deviations from these average values.

Rather than a full derivation of all relevant equations, this Chapter provides foundational context necessary to interpret the research articles presented in this thesis. For an exhaustive formulation of the MHD and kinetic frameworks, we refer the reader to the many comprehensive plasma physics books (Dendy, 1995; Baumjohann & Treumann, 1997; Bellan, 2008; Gurnett & Bhattacharjee, 2017).

### 2.1 Magnetohydrodynamics

In the MHD approach, the plasma is considered as a single fluid. That is, instead of a collection of individual particles, the plasma is treated as a continuum. We can already notice that this approximation breaks down if we consider small-scale processes, where the discrete nature of the particles becomes

**Table 2.1.** Typical solar wind parameters in the inner heliosphere

Parameter	0.3 au	1 au	Description
$\lambda_{De}$	5 m	12 m	Debye length
$\rho_e$	0.6 km	2 km	Electron gyroradius
$\rho_p$	22 km	80 km	Proton gyroradius
$d_e$	0.8 km	2.5 km	Electron inertial length
$d_p$	32 km	100 km	Proton inertial length
$f_{pe}$	63 kHz	20 kHz	Electron plasma frequency
$f_{pp}$	1.5 kHz	0.5 kHz	Proton inertial length
$f_{ce}$	700 Hz	150 Hz	Electron cyclotron frequency ( $1/\tau_{ce}$ )
$f_{cp}$	0.4 Hz	0.1 Hz	Proton cyclotron frequency ( $1/\tau_{cp}$ )
$n_e, n_i$	50 cm <sup>3</sup>	5 cm <sup>3</sup>	Electron, ion density
$V_{sw}^*$	400 km/s	400 km/s	Solar wind speed
$T_e$	20 eV	12 eV	Electron temperature
$T_p^*$	15 eV	8 eV	Proton temperature
$B$	25 nT	5 nT	Magnetic field strength

\*Typical values for slow solar wind.

apparent. Nevertheless, at sufficiently large temporal and spatial scales, the fluid assumption is valid, and we can describe the plasma in terms of a single fluid mass density:

$$\rho_m = \sum_s m_s n_s, \quad (2.1)$$

a center-of-mass velocity:

$$\mathbf{U} = \frac{1}{\rho_m} \sum_s m_s n_s \mathbf{U}_s, \quad (2.2)$$

and a center-of-mass pressure:

$$P = \sum_s P_s. \quad (2.3)$$

The subscript  $s$  indicates particle species. For the species relevant in this thesis,  $s = p$  for protons,  $s = \alpha$  for  $\alpha$ -particles,  $s = i$  for ions in general, and  $s = e$  for electrons. For each species  $s$ , we define the number density  $n_s$ , the bulk velocity vector  $\mathbf{U}_s$ , the partial pressure  $P_s$ , and the particle mass  $m_s$ . The fluid equations, which describe the fluid dynamics, are:

$$\frac{\partial \rho_m}{\partial t} + \nabla \cdot (\rho_m \mathbf{U}) = 0 \quad (\text{mass continuity}) \quad (2.4)$$

$$\rho_m \frac{d\mathbf{U}}{dt} = \mathbf{J} \times \mathbf{B} - \nabla P \quad (\text{momentum}). \quad (2.5)$$

The current density is given by  $\mathbf{J} = \sum_s q_s n_s \mathbf{U}_s$ , where  $q$  indicates the electric charge. The magnetic  $\mathbf{B}$  and electric  $\mathbf{E}$  fields are described by Maxwell's

equations:

$$\nabla \cdot \mathbf{E} = \frac{\rho_q}{\epsilon_0} \quad (\text{Gauss' Law}) \quad (2.6)$$

$$\nabla \cdot \mathbf{B} = 0 \quad (\text{Gauss' Law for Magnetism}) \quad (2.7)$$

$$\nabla \times \mathbf{E} = -\frac{\partial \mathbf{B}}{\partial t} \quad (\text{Faraday's Law}) \quad (2.8)$$

$$\nabla \times \mathbf{B} = \mu_0 \mathbf{J} + \epsilon_0 \mu_0 \frac{\partial \mathbf{E}}{\partial t} \quad (\text{Ampère's Law}) \quad (2.9)$$

where  $\rho_q = \sum_s q_s n_s$  is the net charge density, and  $\epsilon_0$  and  $\mu_0$  denote the permittivity and permeability of free space, respectively. For the fluid description to be valid, MHD assumes that characteristic system timescales are much longer than the collision timescales required for the plasma to reach LTE. Because these timescales are much larger than the time light takes to travel through the system, the displacement current in Ampère's law can be ignored. Furthermore, note that the electric force  $\rho_q \mathbf{E}$  is not present in the momentum equation. This is because of a property of plasmas called quasi-neutrality, which means that  $\rho_q \approx 0$  at scales much larger than  $\lambda_{De}$ . In a plasma, due to the combined effect of the charged particles, the electrostatic potential of a charged particle decays exponentially, with e-folding distance given by  $\lambda_{De}$ . This distance is expressed as:

$$\lambda_{De} = \left( \sum_s \frac{q_s^2 n_s}{\epsilon_0 \kappa_B T_s} \right)^{-1/2} \approx \sqrt{\frac{\epsilon_0 \kappa_B T_e}{q_e^2 n_e}}, \quad (2.10)$$

where the  $\kappa_B$  is the Boltzmann constant and  $T_s$  is the temperature. As a consequence of the quasi-neutrality condition, Gauss's law decouples from the MHD equations, and the induced electric field is derived from Faraday's law and Ohm's law. The latter describes the relation between  $\mathbf{J}$  and  $\mathbf{E}$ . Ohm's law is typically defined through a conductivity  $\sigma$  as:

$$\mathbf{J} = \sigma(\mathbf{E} + \mathbf{U} \times \mathbf{B}), \quad (\text{Ohm's Law}) \quad (2.11)$$

where the term in parentheses represents the electric field in the rest frame of the plasma, expressed in terms of the fields measured in a reference frame where the plasma is moving with velocity  $\mathbf{U}$ , for example, as seen by a spacecraft. In a highly conductive plasma, such as the solar wind, Ohm's law reduces to:

$$\mathbf{E} + \mathbf{U} \times \mathbf{B} = 0. \quad (2.12)$$

Finally, to close the system of MHD equations, an equation of state is used:

$$\frac{d}{dt}(P\rho_m^{-\gamma}) = 0, \quad (\text{Equation of state}) \quad (2.13)$$

where  $\gamma$  is the polytropic index, typically taken as the adiabatic exponent. Equations (2.4), (2.5), (2.7), (2.8), (2.9), (2.12) and (2.13) constitutes the ideal

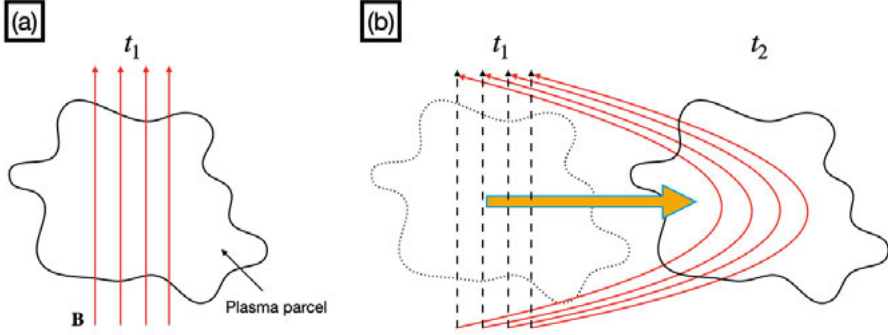


Figure 2.1. The concept of the frozen-in theorem. (a) A plasma parcel embedded in a magnetic field  $\mathbf{B}$  at time  $t_1$ . (b) At time  $t_2$  the system is displaced; the plasma parcel and magnetic field lines move together as if they were frozen to one another. The parameter  $\beta$ , describing the ratio between the plasma thermal pressure and the magnetic pressure, indicates if the motion is dominated by the plasma ( $\beta > 1$ ) or the magnetic field ( $\beta < 1$ ).

MHD equations, describing the coupled dynamics of a conductive fluid and its interaction with electromagnetic fields.

One of the most important results of the MHD equations is that for large  $\sigma$  and large length-scale systems, the magnetic field lines are "frozen" into the plasma (Alfvén, 1942). The frozen-in theorem states that the motion of the magnetic field lines is restricted to follow the motion of the plasma embedded in them, or vice versa, as illustrated in Fig. 2.1. Panel (a) depicts a plasma parcel embedded in a magnetic field. When either the plasma or the magnetic field lines are displaced, the other is dragged along as if they were frozen together, as shown in panel (b). This frozen-in motion is governed by either the magnetic field or the plasma, depending on which exerts a larger pressure. We define the ratio between the plasma thermal pressure and the magnetic pressure as:

$$\beta = \frac{\text{Thermal Pressure}}{\text{Magnetic Pressure}} = \frac{\sum_s n_s \kappa_B T_s}{B^2 / (2\mu_0)}. \quad (2.14)$$

Thus, when  $\beta > 1$  the plasma dictates the motion, and when  $\beta < 1$  it is the magnetic field that dominates the dynamics.

### 2.1.1 Fast and Slow Solar Wind

Applying MHD theory to characteristic parameters of the solar corona, enables a description of the global structure and long-term average properties of both the plasma and the Sun's magnetic field from the corona into interplanetary space. Near the upper chromosphere, the layer of the Sun's atmosphere

immediately beneath the corona, the intense magnetic field results in a low- $\beta$  regime,  $\beta \ll 1$ . Here, the magnetic field, which rotates with the Sun, drags the plasma along with it. In this region, which extends to the upper corona, the plasma co-rotates with the Sun.

The strength of the Sun's magnetic field decreases with radial distance, and  $\beta$  begins to increase, exceeding the  $\beta > 1$  regime. At this point, plasma dominates the dynamics and, as it expands, convects the magnetic field outward. Here, the plasma accelerates radially until it surpasses the local sound and Alfvén velocities,  $V_A = B/\sqrt{\mu_0\rho_m}$  (Parker, 1958; Verscharen et al., 2019). At a radial distance, called the Alfvén radius,  $r_A$ , the plasma becomes super-Alfvénic, and it is no longer magnetically bound to the corona. We note that under typical conditions in the corona, the plasma exceeds the sound speed before reaching  $r_A$ ; consequently, the flow is already supersonic by the time it becomes super-Alfvénic.

The  $r_A$  marks the boundary between the corona and the expanding, radially streaming plasma: the solar wind. The  $r_A$  is not the same at all heliographic longitudes and latitudes, but depends on the plasma and magnetic field conditions at a given time and location. Typically,  $r_A$  ranges between 10-20  $R_\odot$  (Badman et al., 2025), where  $R_\odot = 0.0046$  au is the solar radius.

Plasma that outflows mostly parallel to the magnetic field can escape the corona more easily and do so at a faster velocity. This fast solar wind originates from coronal holes where the magnetic field lines are said to be open—such as the polar regions shown in Fig. 2.2a. Fast solar wind velocity ranges between  $\sim 500$  km/s and 800 km/s (McComas et al., 1998; Verscharen et al., 2019).

On the other hand, plasma originating in regions with predominantly non-radial magnetic fields must carry the field lines outward as it expands, as described by the frozen-in theorem. Consequently, this plasma escapes the corona at lower velocities. Typical slow solar wind velocities range around 300 km/s to 500 km/s (Verscharen et al., 2019). Slow solar wind originates in regions referred to as streamers, such as that found near the equatorial latitudes depicted in Fig 2.2a. Because most in-situ spacecraft missions are confined to the ecliptic plane, the majority of solar wind observations are of plasma originating from equatorial streamers.

### 2.1.2 Parker Spiral and Solar Cycle

The Sun's magnetic field, topologically altered by the solar wind, is known as the interplanetary magnetic field (IMF). Together, the solar wind and the IMF fill the solar system, creating a cavity in the interstellar medium called the heliosphere. To first approximation, the IMF resembles a stretched dipole, like in Fig. 2.2a. This stretched dipole creates a current sheet where the IMF switches polarity, called the heliocentric or interplanetary current sheet.

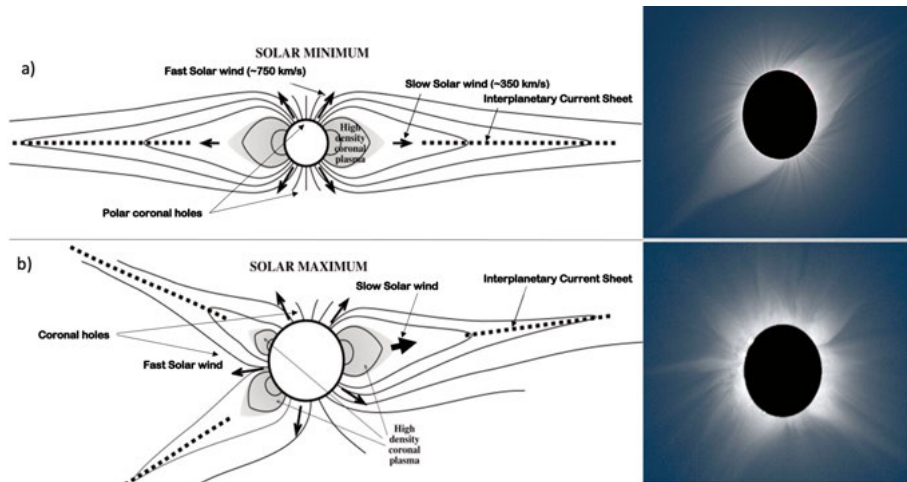


*Figure 2.2.* Two configurations of the solar corona and interplanetary magnetic field (IMF) during a solar cycle. (a) Solar minimum configuration. The fast solar wind is mostly confined to the coronal holes located near polar latitudes; the slow solar wind streams from a belt close to the equator. Right: picture of a solar eclipse during solar minimum. (b) Solar maximum configuration. The coronal magnetic field gets tangled as a result of the Sun's differential rotation. The coronal holes and streamer belts are no longer localized at the poles and equator, respectively. Right: picture of a solar eclipse during solar maximum. Adapted from Lyons (2003). Photographs taken from Dikpati et al. (2016).

Moreover, as the Sun rotates, the points where the magnetic field lines are anchored to the Sun co-rotate with it. However, the stretched section of the IMF is dragged by the solar wind, which flows radially outward from the Sun. This results in the IMF exhibiting a spiral pattern called the Parker spiral, as seen in Fig.2.3.

As the Sun accomplishes more revolutions about its rotation axis, the foot-points of the IMF become increasingly wound and twisted. Over time, the magnetic topology reaches a level of complexity where it no longer resembles a dipole, as illustrated in Fig. 2.2b. As a result, streamer regions and coronal holes are no longer located at the equator and polar regions, respectively. In a lapse of a few years, the accumulated magnetic tension triggers a global reconfiguration, often marked by eruptive events. Eventually, the system is returned to a more quiescent, dipole-like state. This periodic process is called the solar cycle and lasts approximately 11 years.

Solar wind velocity with respect to latitude during two stages of the solar cycle is shown in Fig 2.4. During the solar minimum, illustrated in the left panel, the Sun is in the stretched dipole-like configuration, the streamer region occurs closer to equatorial latitudes, and the coronal holes are mostly confined to the polar regions. In contrast, during solar maximum, shown in the

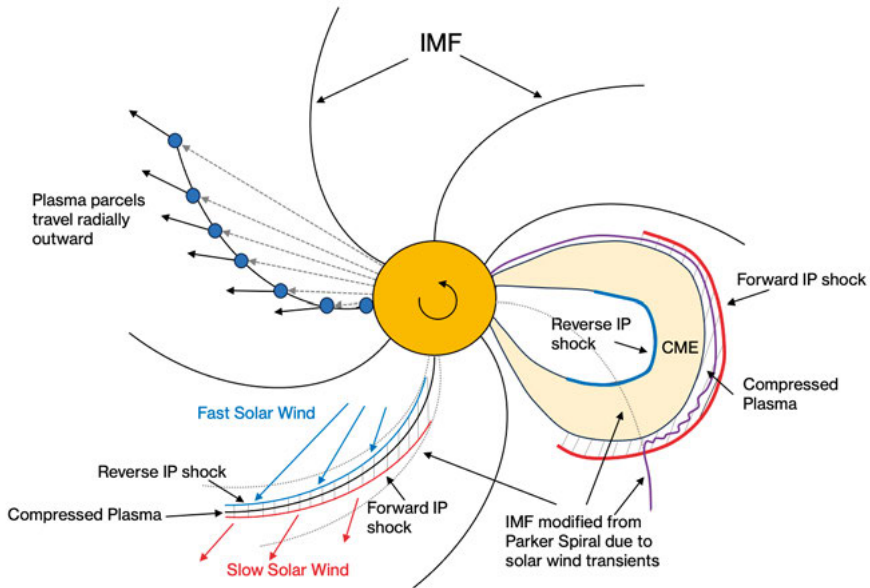


*Figure 2.3.* Parker Spiral and Interplanetary (IP) Shocks. The magnetic field lines are anchored at the solar surface and rotate with the Sun. As the solar wind expands radially, it carries the magnetic field outward; the combination of radial expansion and solar rotation results in the spiral pattern of the IMF. Transient phenomena arise when fast solar wind streams overtake slower flows, forming streaming interaction regions (SIR) where interplanetary shocks can develop. Similarly, during periods of high solar activity, Coronal Mass Ejections (CMEs) are expelled into interplanetary space. These high-speed transients sweep up the preceding plasma, driving IP shocks and distorting the nominal Parker spiral configuration.

right panel, both streamers and coronal holes appear at various latitudes. As a consequence, patches of fast and slow solar wind stream everywhere from the solar corona. Due to the increased complexity of the Sun's magnetic field, coronal activity at solar maximum is significantly more intense and variable than at solar minimum, characterized by more frequent eruptive events that reach the interplanetary medium.

Solar wind observations have revealed that fast solar wind properties are less variable than slow solar wind (Verscharen et al., 2019). Furthermore, the slow solar wind is typically denser, less Alfvénic, and characterized by a shorter collision timescale than the fast solar wind (Marsch et al., 1982; Tu & Marsch, 1995; Kasper et al., 2008).

Ultimately, as the solar wind continues to expand into the outer heliosphere, it eventually becomes subsonic at approximately 100 au as it crosses the termination shock, where the plasma is compressed and heated. Beyond this boundary, the solar wind continues to flow outward until it finally encounters the local interstellar medium at the heliopause. Rather than forming a simple

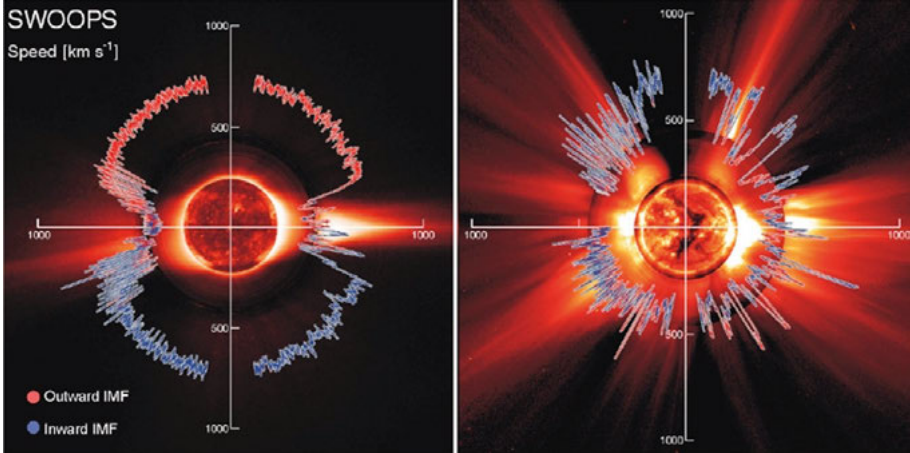


*Figure 2.4.* Solar wind speed observations from the Ulysses spacecraft. (Left) Solar wind speed as a function of heliographic latitude during solar minimum. The solar wind exhibits a highly structured distribution, with steady fast streams at polar regions and slower, more variable flows concentrated near the solar equator. (Right) Solar wind speed as a function of heliographic latitude during solar maximum. The structured latitudinal dependence disappears; instead, contiguous patches of fast and slow wind streams are observed across all latitudes. In both panels, blue lines indicate IMF directed toward the Sun, and red lines indicate an outward orientation. Taken from McComas et al. (2003).

bubble-shaped cavity, recent large-scale MHD models of the heliosphere suggest that the interstellar gas deflects the solar wind into distinct jets directed opposite to the direction of motion of the solar system through the local interstellar medium (Opher et al., 2015, 2020). Therefore, it is safe to conclude that one of the most outstanding successes of MHD models of the solar wind is the realization that we may be flying through the Galaxy inside a giant croissant, as illustrated in Fig. 2.5—almost as if someone was dipping a celestial pastry into the Milky Way. Anyway, even this global configuration remains a subject of active research, as the true shape of the heliosphere is likely more complex, accounting for the intricate footpoint motion of the solar magnetic field (Fisk, 1996; Simnett, 2017). Perhaps future observations will reveal that the heliosphere is actually shaped like a taco.

### 2.1.3 Limitations of the MHD description of the solar wind

While MHD effectively describes the steady global structure of the solar wind, and can account for large-scale turbulence (Mangeney et al., 1991; Galtier & Buchlin, 2007) and very low-frequency waves ( $f \ll f_{ci} = 1/\tau_{ci}$ ) (Rivera et al., 2024), it remains insufficient to explain several common solar wind phenomena. A classic example is the mechanism behind the solar wind acceleration.

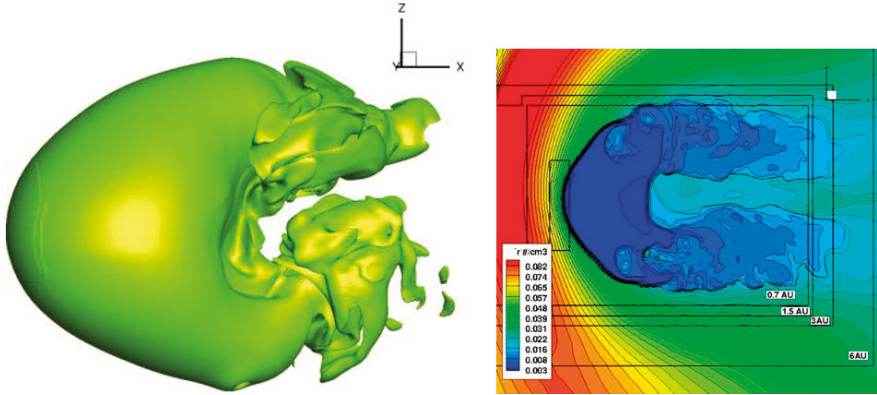
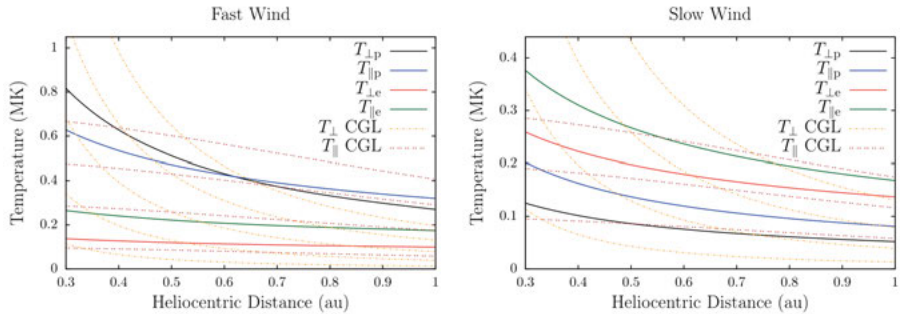


Figure 2.5. Magnetohydrodynamic (MHD) simulation results of the heliosphere and its interaction with the local interstellar medium. (Left) Iso-surface denoting the heliopause, showcasing its two-lobe structure. (Right) Cut in the meridional plane of the simulation, depicting plasma density. These results suggest that we do not live inside a heliosphere, but in a heliocroissant. Taken from Opher et al. (2015).

Within the acceleration region, extending a few  $R_{\odot}$  from the Sun, the solar wind is accelerated until reaching a nearly constant velocity (Barnes, 1992). Most of the velocity gained by the slow solar wind at the acceleration region can be explained within the MHD framework. However, for realistic temperatures in the solar corona, the predicted velocity of the fast solar wind using a pure fluid treatment of the solar wind is not consistent with the observations (Verscharen et al., 2019; Halekas et al., 2022).

Another inconsistency between the MHD solar wind model and the observations is the radial temperature profile of the solar wind. The radial evolution of the solar wind temperatures for fast and slow streams is depicted in Fig 2.6. The solar wind temperature is observed to decrease with distance more slowly than expected from adiabatic expansion, even if we consider different expansion rates across and along the magnetic field (Verscharen et al., 2019). This indicates that MHD models cannot fully account for the solar wind properties as they evolve through the heliosphere, and highlights the necessity of frameworks that include non-adiabatic heating and kinetic processes.

Finally, far from being a steady outflow of plasma, the solar wind exhibits many transient phenomena (Turner et al., 1977; Trotta et al., 2025), turbulence (Alexandrova et al., 2009), and waves (Briand, 2009). Among the most intense solar wind transient phenomena are coronal mass ejections (CME). These are eruptive events that occur when stored magnetic energy in the corona is released, accelerating plasma into the interplanetary medium at velocities reaching up to  $\sim 2000$  km/s (Verscharen et al., 2019). As this high-speed ejecta encounters the slower ambient solar wind, a steep gradient in plasma proper-



*Figure 2.6.* Solar wind temperature radial evolution in the inner heliosphere. (Left) Radial profiles of fast solar wind temperatures parallel ( $T_{\parallel}$ ) and perpendicular ( $T_{\perp}$ ) to the magnetic field. Dashed lines indicate the fluid predictions derived from the double-adiabatic (CGL) equations of state. Solid lines correspond to power-law fits to observed proton and electron temperatures. (Right) Same as (Left) but for slow solar wind. In both regimes, radial temperature profiles derived from observations deviate from the fluid predictions, indicating the presence of non-adiabatic heating and kinetic processes. Taken from Verscharen et al. (2019).

ties forms in the interface, resulting in the formation of an interplanetary (IP) shock. Similarly, IP shocks arise at Stream Interaction Regions (SIRs), where fast solar wind overtake the preceding slow solar wind. Schematic representations of IP shocks formed by CMEs and SIRs are shown in Fig. 2.3. Characterizing the dynamics of IP shocks is essential for space plasma physics, as they drive key solar wind processes, such as particle acceleration (Reames, 2001) and space weather events (Dmitriev et al., 2005).

While the global properties of IP shocks are well-described by MHD theory, under this framework, the shock is treated as a discontinuity between upstream and downstream plasma conditions. As a result, MHD cannot explain processes within the shock transition region. This is primarily due to the small temporal and spatial scales involved, which are on the order of  $\tau_{cp}$  and  $\rho_p$ , respectively. Consequently, the fundamental mechanisms of dissipation required for IP shocks to exist cannot be explained using the MHD approach, as they occur at scales where the fluid approximation is no longer valid.

As indicated, the MHD framework is often insufficient for describing the solar wind evolution. The main limitation of the single-fluid model is its reliance on the assumption of LTE, which is typically achieved through frequent collisions between particles. In the solar wind, however, the high temperatures and low densities result in a collisional mean free path that exceeds the characteristic scales of processes that regulate its state,  $L \ll \lambda_{mfp}$  and  $\tau \ll \tau_{coll}$ . Consequently, the solar wind is classified as a collisionless or weakly collisional plasma. In such a plasma, kinetic processes, namely wave-particle interactions, can dominate the evolution of the system. We discuss wave-particle interactions in Chapter 3.

Some of the limitations of ideal MHD can be overcome by considering specific deviations from LTE. For instance, pressure anisotropies can be incorporated by utilizing the full pressure tensor  $\overleftrightarrow{\mathbf{P}}$  and a modified closure, such as the double-adiabatic (CGL) equations of state; however, this too fails to explain the observed radial evolution of the solar wind temperature. Furthermore, processes occurring at scales near or below  $\rho_i$ , and  $d_i$  can be modeled by accounting for Hall, diamagnetic and inertial effects that arise from electron dynamics when ion dynamics decouple from the magnetic field. In these extended MHD regimes, the relation between  $\mathbf{J}$  and  $\mathbf{E}$  is given by the generalized Ohm's law:

$$\mathbf{E} + \mathbf{U} \times \mathbf{B} = \frac{\mathbf{J}}{\sigma} + \frac{1}{en_e} \mathbf{J} \times \mathbf{B} - \frac{1}{en_e} \nabla \cdot \overleftrightarrow{\mathbf{P}}_e + \frac{m_e}{e^2 n_e} \left[ \frac{\partial \mathbf{J}}{\partial t} + \nabla \cdot (\mathbf{J}\mathbf{U} + \mathbf{U}\mathbf{J}) \right], \quad (2.15)$$

where  $e$  is the elementary charge. Nevertheless, even with these modifications, fluid models cannot describe many non-equilibrium processes, such as high-frequency waves, microinstabilities or wave-particle interactions, that regulate the state of the solar wind in the absence of collisions. To resolve these, we must move beyond fluid models and investigate the solar wind using kinetic theory.

## 2.2 Kinetic Theory

Although kinetic theory, like MHD, does not treat particles as discrete individual entities, it considers the plasma as a statistical representation of particles in phase space. This approach circumvents the limitations of the fluid continuum treatment, allowing for arbitrary deviations from LTE and enabling the analysis of physical processes at much shorter temporal and spatial scales. This phase space is a six-dimensional parameter space describing the three spatial coordinates  $\mathbf{r} = (x, y, z)$  and the three velocity coordinates  $\mathbf{v} = (v_x, v_y, v_z)$ . At any instant of time  $t$ , the dynamical state of a particle is defined by its position  $\mathbf{r}$  and velocity  $\mathbf{v}$  in phase space. Then, the number of particles  $dN$  in a phase space volume element  $(dx, dy, dz, dv_x, dv_y, dv_z)$  is defined by the distribution function  $f(\mathbf{r}, \mathbf{v}, t)$  as follows:

$$dN = f(\mathbf{r}, \mathbf{v}, t) dx dy dz dv_x dv_y dv_z. \quad (2.16)$$

The distribution function describes the phase space density of particles at time  $t$ . Assuming a locally homogeneous and quasi-stationary plasma or an effectively fixed measurement point (e.g., the location of a spacecraft), the spatial and temporal dependencies are neglected; thus,  $f(\mathbf{r}, \mathbf{v}, t)$  reduces to the velocity distribution function (VDF),  $f(\mathbf{v})$ . In LTE, the VDF has the shape of a Maxwellian distribution; however, in the weakly collisional solar wind,

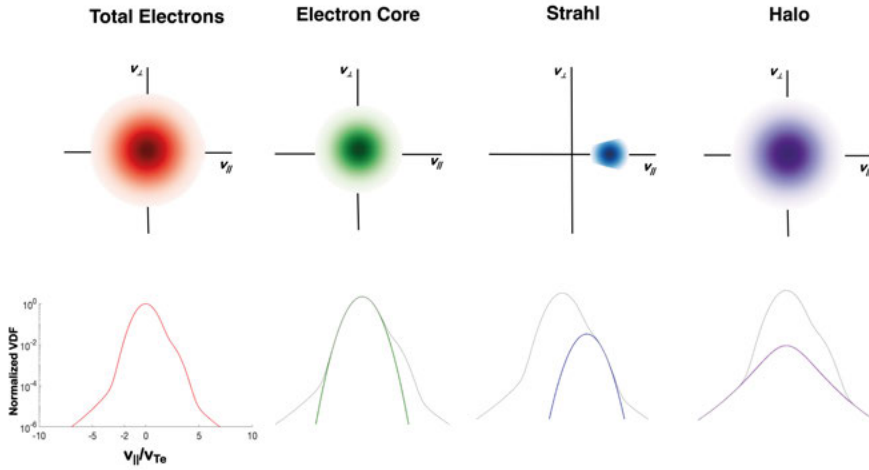


Figure 2.7. Typical electron VDFs in the solar wind. (Top) 2D-VDFs in the  $v_{\parallel}$ - $v_{\perp}$  plane. (Bottom) 1D-VDF along  $v_{\parallel}$ . In red is the total electron VDF. Green corresponds only to the electron core, which constitutes around 95% of the total electrons. The suprathermal halo population is shown in purple and the field-aligned strahl in blue.

many non-Maxwellian features are readily observed in the electron and ion VDFs.

Typical electron VDFs observed in the solar wind are shown in Figs. 2.7. In the top VDFs, the velocity component parallel to the magnetic field,  $v_{\parallel}$ , and one component perpendicular to the magnetic field,  $v_{\perp}$ , are displayed. In the bottom plots, only the VDF along  $v_{\parallel}$  is shown. An important remark is that the VDF is not necessarily the same in all directions. In such cases, it is said that the VDF is anisotropic.

A typical solar wind electron VDF, shown in red in Fig. 2.7, comprises multiple populations. The nearly Maxwellian electrons make up the core population. The core, shown in green, is primarily isotropic and accounts for  $\sim 95\%$  of the total electrons (Feldman et al., 1975; Štverák et al., 2008). According to solar wind kinetic models, such as the exospheric model, the dynamics of the core are closely tied to an interplanetary electric field, generated by a global ambipolar electric potential (Lemaire & Scherer, 1971; Maksimovic et al., 2001). In fluid models, this electric potential manifests as the electron pressure gradient (Parker, 2010). From a kinetic perspective, the core is formed by electrons with insufficient energy to overcome the Sun’s potential well, which extends throughout interplanetary space.

Electrons with enough energy to escape the Sun’s influence form the strahl, shown in blue. These electrons are highly focused into narrow pitch-angle regions in the VDF by the radial decrease in IMF strength, a process known as magnetic or adiabatic focusing (Owens et al., 2008). The strahl is a highly

anisotropic, beam-like population frequently observed in the solar wind. It streams outward from the Sun with a bulk energy of about 100 eV (Verscharen et al., 2019). Although adiabatic focusing acts to narrow the beam as it travels outward, observations show that the strahl’s pitch-angle distribution broadens with heliocentric distance (Rosenbauer et al., 1977; Štverák et al., 2009). In the absence of collisions, this pitch angle scattering suggests that kinetic processes, such as wave-particle interactions, counteract the focusing effect and actively shape the electron VDFs.

The halo population, displayed in purple, is also a nearly isotropic population with a higher proportion of particles at larger velocities compared to a Maxwellian distribution. Often described by a Lorentzian or  $\kappa$ -distribution (Pierrard et al., 2001), the suprathermal halo is believed to originate from the scattering of the strahl through wave-particle interactions (Maksimovic et al., 2005).

Lastly, electron VDFs occasionally exhibit a deficit of particles in the Sunward direction (Halekas et al., 2020). This deficit marks the energy threshold for electron escape and indicates the absence of a high-energy electron source originating from the outer heliosphere. Because the magnitude of the interplanetary electric field is likely below the resolution capabilities of current electric field probes (Halekas et al., 2021), the deficit provides compelling evidence of the Sun’s ambipolar electric potential (Maksimovic et al., 2001; Baby, 2023). The interplanetary electric field is a critical component of solar wind evolution, as it may contribute to the solar wind acceleration (Berčič et al., 2021b). Observations from Solar Orbiter and Parker Solar Probe demonstrate that the deficit is most pronounced at small heliocentric distances (Owen et al., 2022; Baby et al., 2022). Recent studies suggest this feature in the electron VDF is gradually ‘filled’ through pitch-angle scattering of strahl and halo electrons by whistler waves (Berčič et al., 2021a; Verscharen et al., 2022; Micera et al., 2025), suggesting the importance of kinetic processes in shaping the solar wind evolution. Understanding the interaction between these suprathermal populations and the deficit requires a rigorous kinetic treatment and remains a subject of active research.

Just like the electrons, solar wind ions typically consist of several distinct populations, shown in red in Fig. 2.8. The first is a proton core, depicted in green, which, unlike the electron core, tends to be highly anisotropic. While the proton core anisotropy generally exhibits higher velocity spread along  $v_{\perp}$ , intervals of parallel anisotropy also occur (Marsch, 2006; Matteini et al., 2007). A second proton population, shown in blue, streams at higher velocities than the proton core, forming a field-aligned beam (blue). The proton core and beam account for nearly 95% of the solar wind ions.

In addition to protons, solar wind ion VDFs commonly include  $\alpha$ -particles, represented in purple in Fig. 2.8. The  $\alpha$ -particles make up approximately 5% of  $n_i$ , and  $\sim 20\%$  the ion mass density (Ogilvie, 1975). While  $\alpha$ -particles exhibit an anisotropy similar to protons, they are characterized by higher tem-

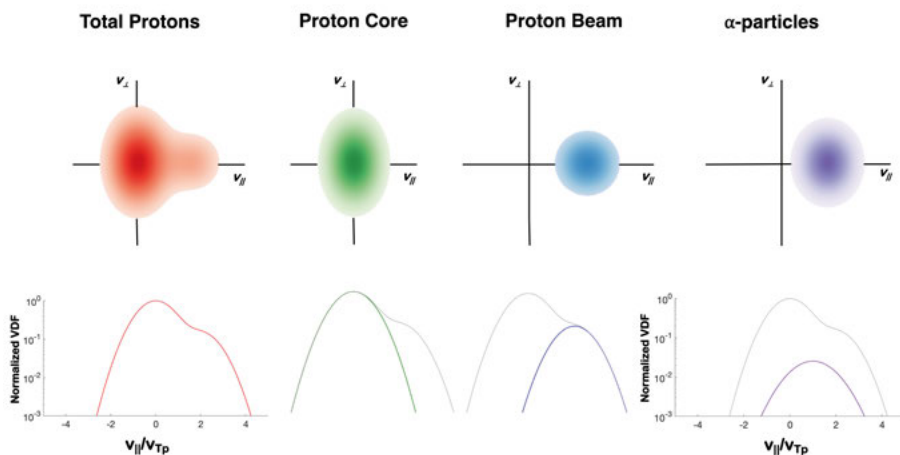


Figure 2.8. Typical ion VDFs in the solar wind. (Top) 2D-VDFs in the  $v_{||}$ - $v_{\perp}$  plane. (Bottom) 1D-VDF along  $v_{||}$ . In red is the total proton VDF. Green corresponds only to the proton core. The proton core often exhibits a  $T_{\perp}/T_{||} > 1$  anisotropy. The proton beam, which is frequently observed in the solar wind, is shown in blue. The  $\alpha$ -particles, which also often exhibit  $T_{\perp}/T_{||} > 1$  are shown in purple. The ions in the solar wind are typically anisothermal, meaning that the temperatures of different ion species are not the same. In the solar wind  $T_{\alpha} > T_p$ .

peratures, often exceeding four times that of protons (Chandran et al., 2013). Furthermore,  $\alpha$ -particles tend to drift faster than the proton core; however, this relative velocity gradually decreases with heliocentric distance (Reisenfeld et al., 2001), and is likely regulated by kinetic instabilities (Verscharen et al., 2015). Finally, traces of heavier ions,  $\lesssim 1\%$  of  $n_i$ , such as oxygen, carbon, or iron, are also present in the solar wind (Ogilvie & Coplan, 1995).

The evolution of the solar wind distribution function is dictated by the Vlasov-Maxwell equation:

$$\frac{\partial f_s(\mathbf{r}, \mathbf{v}, t)}{\partial t} + \mathbf{v} \cdot \nabla f_s(\mathbf{r}, \mathbf{v}, t) + \frac{q_s}{m_s} (\mathbf{E} + \mathbf{v} \times \mathbf{B}) \cdot \nabla_v f_s(\mathbf{r}, \mathbf{v}, t) = 0, \quad (2.17)$$

where the symbol  $\nabla_v$  means the gradient over velocity space. The Vlasov-Maxwell equation describes the evolution of the distribution function of particle species  $s$  under the effect of the Lorentz force  $q_s(\mathbf{E} + \mathbf{v} \times \mathbf{B})$  and in the absence of collisions. The evolution of the electric and magnetic fields is described by Maxwell's equations (2.6)–(2.9).

The kinetic state of the plasma can be connected to macroscopic quantities by taking averages of the VDF. The most common averages used are obtained by multiplying the VDF by powers of  $\mathbf{v}$  and integrating over velocity space. These averages are referred to as moments of the distribution. The first four

moments of the VDF are:

**Zeroth moment (number density)**

$$n_s = \int_{\mathbf{v}} f_s(\mathbf{v}) dv_x dv_y dv_z,$$

**First moment (bulk velocity vector)**

$$\mathbf{U}_s = \frac{1}{n_s} \int_{\mathbf{v}} \mathbf{v} f_s(\mathbf{v}) dv_x dv_y dv_z,$$

**Second moment (Pressure tensor)**

$$\overleftrightarrow{\mathbf{P}}_s = m_s \int_{\mathbf{v}} (\mathbf{v} - \mathbf{U}_s)(\mathbf{v} - \mathbf{U}_s) f_s(\mathbf{v}) dv_x dv_y dv_z,$$

**Third moment (Heat-flux tensor)**

$$\overleftrightarrow{\mathbf{Q}}_s = m_s \int_{\mathbf{v}} (\mathbf{v} - \mathbf{U}_s)(\mathbf{v} - \mathbf{U}_s)(\mathbf{v} - \mathbf{U}_s) f_s(\mathbf{v}) dv_x dv_y dv_z,$$

where  $\overleftrightarrow{\mathbf{P}}_s$  and  $\overleftrightarrow{\mathbf{Q}}_s$  are defined in the rest frame of the species  $s$ , making them centered moments. Furthermore, the temperature tensor  $\overleftrightarrow{\mathbf{T}}_s$  is related to  $\overleftrightarrow{\mathbf{P}}_s$  through  $\overleftrightarrow{\mathbf{P}}_s = n_s \kappa_B \overleftrightarrow{\mathbf{T}}_s$ . This  $\overleftrightarrow{\mathbf{T}}_s$  characterizes the velocity spread of the VDF and is not necessarily isotropic, meaning temperature values can differ depending on the direction. For VDFs in LTE,  $\overleftrightarrow{\mathbf{T}}_s$  reduces to a scalar  $T_s$ , which is used to define the thermal speed,  $v_{T_s} = \sqrt{2\kappa_B T_s / m_s}$ , which characterizes the width of the Maxwellian distribution.

For anisotropic VDFs where  $\overleftrightarrow{\mathbf{T}}_s$  is diagonal, such as a bi-Maxwellian distribution, distinct  $v_{T_s}$  can be defined for each principal direction. However, for more complex distributions with  $\overleftrightarrow{\mathbf{T}}_s$  containing off-diagonal components, the tensor must be rotated into the principal frame (Richard et al., 2025)—where the tensor is strictly diagonal—to extract a physical meaning closer to the concept of thermodynamic temperature, which is related to the mean kinetic energy. In this frame, the diagonal elements represent the temperatures along the principal axes; in the solar wind, one axis of the principal frame is usually aligned with the local magnetic field.

When measuring different particle species, the distinct VDFs of each species have different implications for ions and electron spacecraft measurements. For ions  $v_{Ti} \ll \mathbf{U}_i$ , causing them to appear as a highly directed cold beam traveling away from the Sun near the  $\mathbf{E} \times \mathbf{B}$ -drift velocity. In contrast,  $v_{Te} > \mathbf{U}_e$ , resulting in electrons detected from all directions.

Macroscopic quantities in a collisionless plasma are significantly influenced by kinetic processes, which are themselves determined by the shape of the VDFs. In the solar wind environment, the various particle species and populations interact with electromagnetic fields across a wide range of temporal

and spatial scales. These interactions trigger kinetic mechanisms that are fundamental for constraining deviations from LTE and regulating the evolution of the solar wind. The following sections detail the specific kinetic-scale phenomena investigated in the papers included in this thesis.

### 2.2.1 Ion-scale Kinetics

Ion-scale processes typically refer to phenomena occurring at spatial scales comparable to the ion gyroradius ( $\rho_i = v_{\perp}/\omega_{ci}$ ), and the ion inertial length ( $d_i = c/\omega_{pi}$ ), but above the electron gyroradius ( $\rho_e = v_{\perp}/\omega_{ce}$ ), and electron inertial length ( $d_e = c/\omega_{pe}$ ). In time, these processes develop on scales spanning the range between the ion gyroperiod ( $\tau_{ci} = 2\pi/\omega_{ci}$ ) and the ion plasma period ( $\tau_{pi} = 2\pi/\omega_{pi}$ ). Here, the plasma frequency for species  $s$  is defined as:

$$\omega_{ps} = \frac{q_s^2 n_s}{\epsilon_0 m_s}. \quad (2.18)$$

Likewise, the cyclotron frequency is given by:

$$\omega_{cs} = \frac{|q_s| B}{m_s}. \quad (2.19)$$

This range defines the transition when ion inertial and gyration effects dominate the plasma dynamics, before electron kinetic effects become significant at even shorter scales. At kinetic ion-scales, many processes involving ion VDFs take place. Many of these ion-scale processes facilitate the coupling between smaller and larger scales. Hence, ion kinetics are an important link in the multi-scale evolution of the solar wind, bridging the gap between large-scale fluid dynamics and small-scale electron physics. The relevant ion-scale phenomena for this thesis are:

#### Magnetic Holes

Magnetic holes (MH) are localized depressions in the magnetic field magnitude relative to the ambient background (Turner et al., 1977). They are frequently observed in the solar wind as ion-scale structures with widths comparable to  $\rho_p$ , although both larger and smaller-scale MHs have also been documented (Volwerk et al., 2020). Figure 2.9 shows an example of a MH identified in solar wind data. Based on their magnetic topology, these structures are broadly classified into rotational and linear MHs. Rotational MHs are associated with a rotation of the magnetic field vector components, while linear MHs exhibit nearly constant field orientation. By convention, linear MHs are defined by a rotation of less than  $10^{\circ}$ – $15^{\circ}$  between the edges of the depression (Tsurutani et al., 2011; Madanian et al., 2020; Karlsson et al., 2021).

The origin of MHs remains a subject of ongoing research, but they are proposed to be remnants of mirror-mode storms, which consist of a continuous

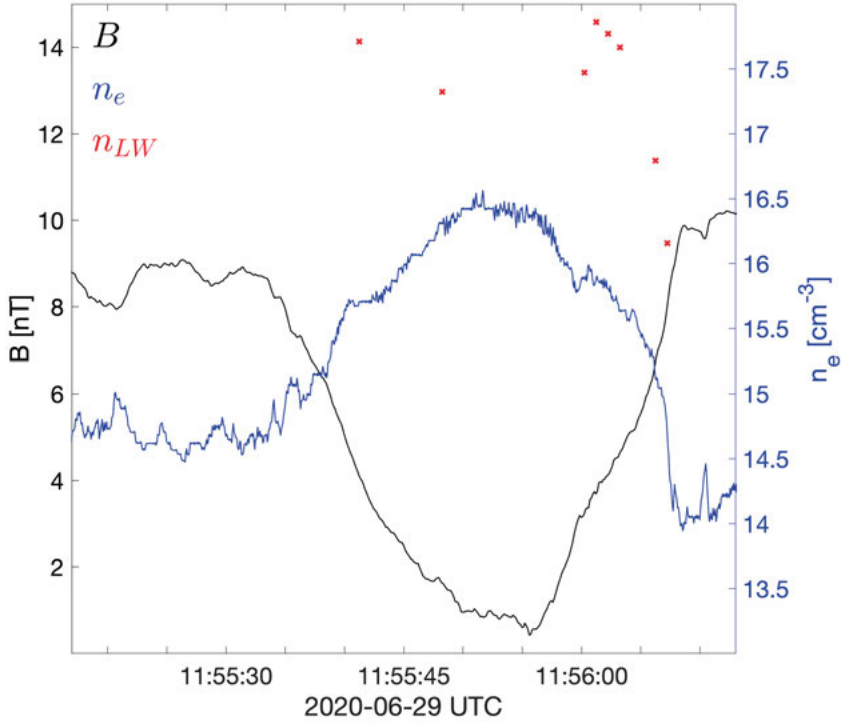


*Figure 2.9.* A magnetic hole observed by Solar Orbiter. Left axis in black: the magnetic hole is characterized by its decrease in magnetic field magnitude. Right axis in blue: the density profile around the magnetic hole. A localized enhancement in density is a common feature of solar wind magnetic holes. The red x-marks indicate the density estimated from the peak frequency of Langmuir waves. All of the Langmuir waves observed in this interval occur inside the magnetic hole.

series of magnetic fluctuations arising from temperature anisotropies (Winterhalter et al., 1994). A key feature of MHs is that they are typically in pressure balance with the surrounding plasma. As a consequence, the magnetic field depression is compensated by a localized enhancement in plasma pressure, often manifested as a density increase, as shown in Fig. 2.9.

Observations at 1 au have identified significant wave activity within MHs, most notably Langmuir waves (Lin et al., 1996; Briand et al., 2010). Through the excitation of these waves, MHs can facilitate the development of wave-particle interactions; for instance, Langmuir waves can modify the solar wind electron VDFs via Landau damping (Baumjohann & Treumann, 1997), a kinetic process discussed in Chapter 3. In paper I, we calculate the occurrence rate of Langmuir waves in the solar wind and identify those associated with MHs. Our findings indicate that Langmuir waves are statistically more likely

to occur in localized regions where the magnetic field magnitude is lower and the density is larger than the background levels.

The enhanced Langmuir wave activity within magnetic depressions suggests a cross-scale coupling between ion-scale structures and electron-scale processes. While the specifics of the generation mechanism for these waves remains under debate, theories involve the violation of the first adiabatic invariant of strahl electrons (Liu et al., 2025). In this way, MHs may play a role in the evolution of the electron VDFs by the scattering of the strahl.

## Interplanetary Shocks

Although the full extension of IP shocks spans distances much larger than ion-scales, the shock transition itself occurs over a width on the order of  $\rho_p$ . Interplanetary shocks are characterized by abrupt jumps in solar wind properties, such as bulk velocity, density, and magnetic field magnitude. Interplanetary shocks are classified as forward if they propagate away from the Sun relative to the solar wind, or reverse if their propagation direction relative to the solar wind is Sunward. Generally, forward shocks form at the leading edges of CMEs or SIRs, while reverse shocks tend to develop at the trailing edges, as illustrated in Fig. 2.3. The majority of the IP shocks observed at 1 au are forward shocks (Kilpua et al., 2015).

An example of spacecraft data showcasing an IP shock is shown in Fig. 2.10. The narrow region of the shock containing the abrupt jump is known as the shock ramp, which separates the unshocked upstream plasma from the compressed and heated downstream plasma. Due to the different responses of ions and electrons upon entering the ramp, occurring at their respective gyroradius and gyroperiod scales, a charge separation develops across the transition. This separation results in a cross-shock potential drop and a corresponding electric field directed along the shock normal, pointing upstream.

Several key parameters that describe the nature of IP shocks can be defined from macroscopic quantities. The Alfvén Mach number,  $M_A$ , is the ratio between the upstream flow velocity (in the shock rest frame and in the direction normal to the shock surface) and  $V_A$ . As  $M_A$  provides insight into the onset of various physical mechanisms, it serves as an indicator for processes occurring around the shock. For instance, low- $M_A$  shocks are typically characterized by laminar and stationary behavior (Mellott, 1985), whereas the high- $M_A$  regime is dominated by non-stationary and non-linear processes (Johlander et al., 2016; Gingell et al., 2017; Khotyaintsev et al., 2024). However, recent studies have shown that even at low- $M_A$  shocks, kinetic effects can lead to turbulent activity (Wilson III et al., 2017; Graham et al., 2024; Graham & Khotyaintsev, 2025, paper III).

Another important parameter is the shock normal angle,  $\theta_{Bn}$ , defined as the angle between the upstream magnetic field and the shock normal direction. The plasma dynamics and electromagnetic field profiles vary significantly depending on  $\theta_{Bn}$ . Generally, shocks with large  $\theta_{Bn}$  exhibit a sharp, well-defined

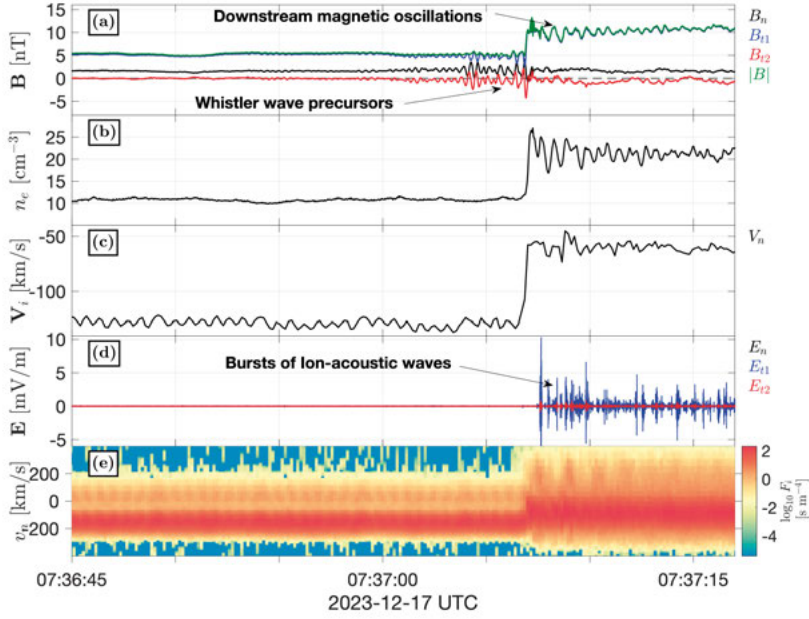


Figure 2.10. An example of spacecraft data of an IP shock, characterized by jumps or discontinuities in density, bulk velocity and magnetic field. The  $\hat{n}$ -axis is in the shock normal direction, the  $\hat{t}_2$  is perpendicular to the magnetic field vector and  $\hat{n}$ , and  $\hat{t}_1$  completes the right-hand system. (a) Magnetic field components and magnitude. (b) Electron density. (c) Component along  $\hat{n}$  of the ion bulk velocity. (d) Electric field components high-pass filtered above 100 Hz. (e) 1D-reduced VDF along  $\hat{n}$ . Various wave modes are observed in the vicinity of the shock. In panel (e), protons and  $\alpha$ -particles are seen well separated in the upstream region.

ramp. In contrast, shocks with normal direction more aligned to the upstream magnetic field tend to be more turbulent, displaying a wider transition between upstream and downstream regions (Balogh & Treumann, 2013). Moreover, the compression ratios  $B_d/B_u$  and  $n_d/n_u$ , which scale with  $M_A$ , quantify the jump in the magnetic field and density from the upstream to the downstream regions.

For shocks to exist, some kind of energy dissipation is required in order to counteract the nonlinear steepening of the wavefront. In the fluid description, without such dissipation, the wavefront eventually ‘breaks’ as the spatial gradients of the plasma parameters, such as density and magnetic field strength, steepen until they become non-physical (Balogh & Treumann, 2013). While in neutral gases and collisional plasmas, the dissipation is controlled by particle collisions, collisionless plasmas must rely on other channels of energy dissipation, such as the wave-particle interactions described by kinetic theory.

Of particular interest are electrostatic waves, which can provide the required dissipation mechanisms at IP shocks through their interaction with particles.

These wave-particle interactions modify the VDFs, playing the role of particle collisions. Therefore, investigating the waves that emerge in the vicinity of collisionless shocks is essential for understanding the fundamental physics of energy dissipation in the solar wind.

For collisionless shocks where  $M_A$  exceeds a critical value ( $M_{A,crit} \approx 2.7$ ), the large input energy from the upstream flow cannot be dissipated by wave-particle interactions alone (Balogh & Treumann, 2013). Beyond this threshold, the shock begins to reflect a fraction of the incident ions back into the upstream region to remove the excess energy. This reflected ion population forms a beam that can either escape upstream or cross downstream. In the latter case, the reflected ions are accelerated in the upstream region by the convection electric field ( $\mathbf{E} = -\mathbf{U} \times \mathbf{B}$ , eq. (2.12)) as they gyrate, eventually forming a secondary ion population upon being transmitted into the downstream region (Wilkinson et al., 2023). In both cases, the newly formed ion population can lead to instabilities that excite waves and alter the shock structure. For even larger- $M_A$  shocks, more complex non-stationary phenomena, such as rippling (Johlander et al., 2016; Gingell et al., 2017; Khotyaintsev et al., 2024) and reformation (Chapman et al., 2005; Lefebvre et al., 2009) are triggered.

In contrast, IP shocks typically exhibit low  $M_A$ , though CME-driven shocks often reach the high- $M_A$  regime (Trotta et al., 2025). These sub-critical shocks allow for the investigation of ion kinetic behavior in an environment where ion reflection does not obscure the underlying dynamics of the core populations. An example is the presence of downstream magnetic oscillations, which are related to fluctuations in the VDF of ions that are directly transmitted across the shock (Gedalin et al., 2018; Graham & Khotyaintsev, 2025).

These downstream oscillations appear when a cold ion population, such as solar wind ions, encounters a shock. Upon crossing the ramp, the ion cyclotron motion becomes more pronounced, due to the larger downstream magnetic field and the deceleration by the cross-shock electric field. An example of an ion trajectory across the shock is illustrated in Fig. 2.11. If the ion temperature is sufficiently low, the distribution gyrates as a coherent whole, causing its moments to fluctuate at a frequency near  $\omega_{ci}$ . Under the condition of total pressure balance, the plasma pressure fluctuations are compensated by the magnetic pressure, giving rise to the downstream magnetic oscillations.

In paper III, through a detailed kinetic analysis of an IP shock, we identify the origin of downstream magnetic oscillations and link them to fluctuations in the VDFs of protons transmitted directly across the shock. While the relationship between downstream magnetic oscillations and gyrating populations of directly transmitted ions has been demonstrated for other types of collisionless shocks, such as planetary bow shocks (Balikhin et al., 2008; Graham et al., 2024), this connection had previously remained largely speculative for IP shocks.

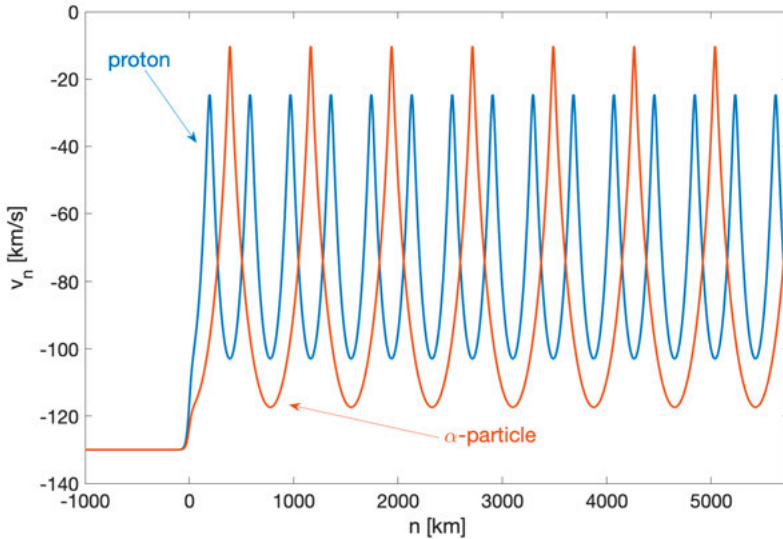


Figure 2.11. Velocity in the shock-normal direction of a proton (blue) and an  $\alpha$ -particle (red) as they cross a quasi-perpendicular shock ( $\theta_{Bn}=70^\circ$ ). The x-axis denotes the distance in the shock-normal direction where  $n = 0$  km at the ramp. Both ions approach from the left at the  $\mathbf{E} \times \mathbf{B}$ -drift velocity. The larger magnetic field downstream and deceleration by the cross-shock electric field produce the pronounced cycloid motion.

The example shock in Fig. 2.10 exhibits a low  $M_A \approx 3$  and features a variety of wave modes in the vicinity of the ramp. Within and around the ramp, strong electrostatic waves are frequently observed (Wilson III et al., 2007). These waves can potentially provide the necessary dissipation for the shock to exist. In particular, ion-acoustic waves are a likely candidate for providing this energy dissipation, as they are commonly detected near IP shocks at 1 au and beyond (R. A. Hess et al., 1998). In paper II, we calculate the occurrence rate of ion-acoustic waves observed near IP shocks in the inner heliosphere.

## 2.2.2 Electron-scale Kinetics

At even smaller scales, comparable to  $\rho_e$  and  $d_e$ , electron dynamics dominate many plasma processes. These processes occur on time scales shorter than  $\tau_{pi}$ , reaching frequencies that approach or exceed the electron cyclotron frequency  $\omega_{ce}$  and the ion plasma frequency  $\omega_{pi}$ . Many microinstabilities and their associated kinetic wave modes emerge at these scales, which can modify both electron and ion VDFs in the solar wind. The electron-scale processes relevant to this thesis include:

## Wave-particle interactions

Plasma waves represent one of the primary mechanisms for regulation of the electron and ion VDFs in the solar wind. Kinetic waves are triggered when a VDF resides in an unstable configuration. Then, the electrostatic or electromagnetic fluctuations exchange energy with the charged particles, diffusing them in velocity space. The overall effect of the waves results in a reconfiguration of the VDF toward a higher entropy state. The cumulative effect of these kinetic-scale changes in the VDFs ultimately contributes to the evolution of the macroscopic properties of the solar wind.

Many electron-scale kinetic waves are frequently observed in the solar wind. Common solar wind electromagnetic waves include whistlers (Tong et al., 2019; Kretschmar et al., 2021), while electrostatic waves include Langmuir (Kellogg et al., 1999; Briand, 2015) and ion-acoustic waves (Gurnett & Frank, 1978; Briand, 2009). Each of these wave modes is driven by distinct instabilities and is characterized by unique dispersion relations (Gary, 1993).

As detailed in Chapter 3, part of this thesis focuses on the properties of some of these wave modes and the instabilities from which they originate. Specifically, we investigate high-frequency electrostatic Langmuir and ion acoustic waves. These modes are often associated with transient solar wind structures, such as MHs (Lin et al., 1996; Briand et al., 2010) or IP shocks (R. A. Hess et al., 1998; Wilson III et al., 2007).

## Radio Bursts

Radio bursts are electromagnetic emissions of the free propagating wave branches, which are generated by the decay of Langmuir waves (Melrose, 1980; Cairns et al., 2003). A spectrogram of the electric field power spectral density (PSD), showcasing radio bursts, is shown in Fig 2.12. The radio burst appears as an increase in PSD that drifts toward lower frequencies over time. Occasionally, Langmuir waves are detected below the radio emissions, providing evidence that the spacecraft is probing the source region directly.

The Langmuir waves that produce the radio bursts are generated by fast suprathermal electron beams. These Langmuir waves are subsequently converted, via linear mode conversion or non-linear wave-wave interactions, into freely propagating Ordinary or Extraordinary electromagnetic modes, which can be observed remotely (Graham & Cairns, 2013, 2014). Depending on the origin of the beams of accelerated electrons, radio bursts exhibit different spectral characteristics (Wild & Smerd, 1972). The two types of radio bursts discussed in this thesis are:

- **Type II:** Radio bursts triggered by electrons accelerated at the shock front of IP shocks, typically those driven by CMEs.
- **Type III:** More frequently observed radio bursts that originate from electrons accelerated during solar flares in the solar corona. Due to the high velocity of the solar flare beams, Type III bursts are characterized by much faster frequency drifts compared to Type II bursts.

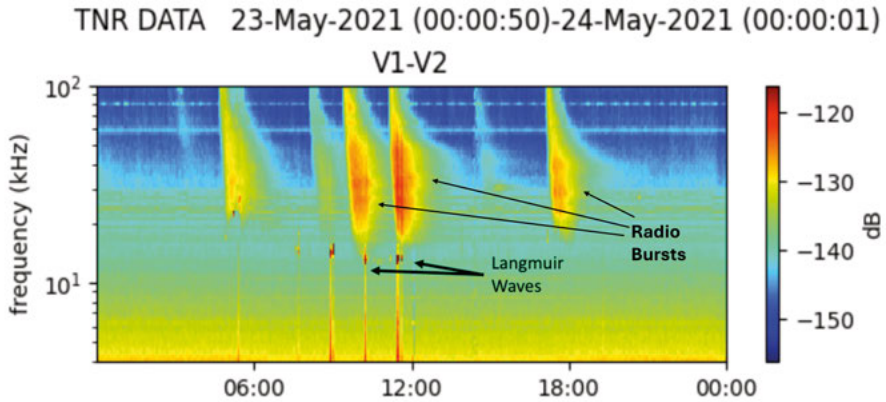


*Figure 2.12.* Electric field dynamic spectra showing a series of Type III radio bursts captured by Solar Orbiter. The radio burst is recognized by its enhancement in power at radio frequencies. Langmuir waves are observed at the base of the radio burst, close to the electron plasma frequency. Retrieved and adapted from: <https://rpw.lesia.obspm.fr/rpw-data/daily-summary-plots/>

In paper I, we identify and distinguish Langmuir waves associated with radio bursts from those unrelated to such emissions. We find that Langmuir waves associated with radio bursts exhibit significantly larger amplitudes. While radio-burst Langmuir waves are generated by transient, accelerated electron beams, the non-radio-burst Langmuir waves are likely associated with the electron strahl.

### 3. Kinetic Waves

Kinetic plasma waves are believed to be among the major drivers in the evolution of the solar wind parameters. These waves reshape the VDFs in the solar wind by relaxing any unstable configuration. It is important to note that even in the absence of collisions, the Vlasov-Maxwell system supports stable non-Maxwellian equilibria; thus, a non-Maxwellian feature in the VDFs does not guarantee the onset of an instability. Nevertheless, distinct instabilities—and the wave modes they excite—are triggered by sources of free energy, which typically involve temperature anisotropies, beams, or secondary populations within the VDFs. Therefore, the observation and identification of particular wave modes serve as a diagnostic tool for the underlying solar wind physics.

Plasma waves analyzed within the kinetic framework are described using the Vlasov-Maxwell equation (2.17). In this Chapter, rather than providing a rigorous derivation, we summarize the fundamental steps of kinetic wave analysis. We focus on electrostatic wave theory, as these wave modes constitute the main subject of this thesis. For a more detailed description of the kinetic treatment of plasma waves, the reader is referred to standard plasma physics literature (Stix, 1992; Swanson, 2020; Treumann & Baumjohann, 1997; Gurnett & Bhattacharjee, 2017).

In linear wave theory, the plasma is described by a homogeneous, stationary background VDF  $f_{s0}$  and a small-amplitude perturbation  $f_{s1}$ , such that the total distribution function of species  $s$  is expressed as:

$$f_s(\mathbf{r}, \mathbf{v}, t) = f_{s0}(\mathbf{v}) + f_{s1}(\mathbf{r}, \mathbf{v}, t). \quad (3.1)$$

Similarly, the electromagnetic fields, which are governed by Maxwell's equations, are decomposed into a background state and a small-amplitude perturbation. To solve the coupled system of Vlasov and Maxwell's equations, we apply a Fourier transform in the space variable  $\mathbf{r}$ . The resulting set of ordinary differential equations is subsequently solved as an initial value problem using a Laplace transform in the time variable  $t$ . This approach treats the perturbations as a superposition of elementary plane waves  $e^{i(\mathbf{k}\cdot\mathbf{r}-\omega t)}$ , where  $\omega$  is the angular frequency and  $\mathbf{k}$  is the wave vector indicating the direction of propagation.

Under this framework, the frequency is generally treated as a complex quantity,  $\omega = \omega_r + i\gamma$ . The real part,  $\omega_r$ , corresponds to the wave frequency, and the imaginary part,  $\gamma$ , represents the growth or damping rate. If  $\gamma > 0$ , the wave amplitude grows exponentially, indicating an instability extracts energy from

the VDF; conversely, if  $\gamma < 0$ , the wave is damped, transferring its energy back to the particles.

The linear response of the plasma to the electromagnetic fields can be expressed through Ohm's law:

$$\mathbf{J} = \overleftrightarrow{\sigma} \cdot \mathbf{E}, \quad (3.2)$$

where  $\overleftrightarrow{\sigma}$  is the conductivity tensor. In the general case, wave solutions are characterized by an effective dielectric tensor  $\overleftrightarrow{\mathbf{K}}$ . The effective dielectric tensor is related to  $\overleftrightarrow{\sigma}$  in  $(\mathbf{k}, \omega)$  space as:

$$\overleftrightarrow{\mathbf{K}} = [I_{3 \times 3}] - \frac{\overleftrightarrow{\sigma}}{i\omega\epsilon_0}, \quad (3.3)$$

where the matrix  $I_{3 \times 3}$  is the unit tensor.

In a source-free system, Maxwell's equations can be rearranged in the  $(\mathbf{k}, \omega)$  domain to yield the homogeneous wave equation:

$$\mathbf{k} \times (\mathbf{k} \times \tilde{\mathbf{E}}_1) + \frac{\omega^2}{c^2} \overleftrightarrow{\mathbf{K}} \cdot \tilde{\mathbf{E}}_1 = \mathbf{0}, \quad (3.4)$$

where  $\tilde{\mathbf{E}}_1$  is the small perturbation of the electric field in  $(\mathbf{k}, \omega)$  space. Equation (3.4) can be expressed in terms of the dispersion matrix  $\mathbf{D}(\mathbf{k}, -i\omega)$  as:

$$\left[ \frac{c^2}{\omega^2} (\mathbf{k}\mathbf{k} - k^2[I_{3 \times 3}]) + \overleftrightarrow{\mathbf{K}} \right] \cdot \tilde{\mathbf{E}}_1 \equiv \mathbf{D}(\mathbf{k}, -i\omega) \cdot \tilde{\mathbf{E}}_1 = \mathbf{0}, \quad (3.5)$$

where  $\mathbf{k}\mathbf{k}$  indicates dyadic product. The term in parentheses involving  $c^2/\omega^2$  indicates the electromagnetic properties of a wave in a vacuum, whereas  $\overleftrightarrow{\mathbf{K}}$  corresponds to the contributions from the plasma response to the fluctuating fields. For non-trivial solution ( $\tilde{\mathbf{E}} \neq 0$ ), the determinant of  $\mathbf{D}(\mathbf{k}, -i\omega)$  must satisfy:

$$D(\mathbf{k}, -i\omega) = 0. \quad (3.6)$$

This equation is known as the dispersion relation. Its roots provide the permitted wave modes that can propagate in the plasma medium with properties determined by  $\overleftrightarrow{\mathbf{K}}$ .

The propagation properties of a specific wave mode are given by  $D(\mathbf{k}, -i\omega)$ , which establishes the dependence of  $\omega$  on  $\mathbf{k}$ . Wave fronts of constant phase propagate at the phase velocity  $\mathbf{v}_{\text{ph}} = (\omega/|\mathbf{k}|)\hat{\mathbf{k}}$ . This means that a particle traveling at  $\mathbf{v} = \mathbf{v}_{\text{ph}}$  experiences a constant wave phase. This condition defines the Landau resonance, one of the fundamental mechanisms for wave-particle interactions. The condition for Landau resonance in an unmagnetized plasma is expressed in terms of a particle's resonance velocity  $\mathbf{v}_{\text{res}}$  as:

$$\mathbf{k} \cdot \mathbf{v}_{\text{res}} = \omega_r. \quad (3.7)$$

Overall, particles moving slightly faster than  $\mathbf{v}_{res}$  transfer some of their energy to the wave. On the other hand, particles moving slightly slower than  $\mathbf{v}_{res}$  extract energy from the wave. Consequently, VDFs with a greater number of particles just above  $\mathbf{v}_{res}$  than below exhibit a ‘positive slope’ that produces kinetic instabilities driving the growth of wave modes. In contrast, when the VDFs contain a higher number of particles just below  $\mathbf{v}_{res}$  than above, the waves will undergo Landau damping. Moreover, if  $\mathbf{v}_{ph}$  lies far in the VDF tail, the population of resonant particles becomes increasingly small. In this non-resonant regime, since very few particles in the VDF travel at  $\mathbf{v}_{ph}$ , wave-particle interactions are effectively suppressed.

In the presence of a background magnetic field  $\mathbf{B}_0$ , particles gyrate at  $\omega_{cs}$ . Then, an additional resonance, the cyclotron resonance, occurs if a particle experiences the wave field oscillating at  $\omega_{cs}$  or at a harmonic of this frequency. However, the particles’ parallel motion along  $\mathbf{B}_0$  introduces a Doppler shift to the wave frequency in the particle’s frame. Consequently, particles interact with the wave most strongly when  $v_{||} = v_{res}$ , matching the Doppler shifted cyclotron resonance condition:

$$\omega_r - k_{||}v_{res} = n\omega_{cs}, \quad (3.8)$$

where  $n$  is an integer ( $0, \pm 1, \pm 2, \pm 3 \dots$ ) representing the harmonic number of  $\omega_{cs}$ . The case where  $n = 0$  corresponds to Landau resonance for a magnetized plasma, driven by the parallel wave electric field  $E_{||,1}$ , and Barnes resonance, driven by the mirror force created by the parallel gradient of the wave magnetic field strength  $\nabla_{||}B_1$ . For electrostatic modes, there is no magnetic component of the wave, and the  $n = 0$  resonance condition is strictly provided by Landau damping.

To define the VDF instability condition for the onset of a kinetic wave mode, we introduce the reduced distribution function:

$$F_{0s}(v_{||}) = \frac{1}{n_{0s}} \iint_{-\infty}^{\infty} f_{0s} dv_{\perp,1} dv_{\perp,2}, \quad (3.9)$$

remembering that the subscript 0 denotes the stationary background quantity. This reduction is performed along the axis parallel to the background magnetic field. The VDF instability condition for Landau resonance in a magnetized plasma is written in terms of the slope of  $F_0$  as:

$$\left. \frac{\partial F_{0s}(v_{||})}{\partial v_{||}} \right|_{v_{||}=v_{res}} > 0. \quad (3.10)$$

This indicates that to drive a kinetic instability through Landau resonance, a positive slope in  $F_{0,s}$  along  $v_{||}$  is needed. In contrast, unlike Landau resonance, cyclotron resonances are often driven by temperature anisotropies or gradients in the perpendicular velocity space. Consequently, the stability of the VDF is more commonly analyzed within the framework of quasi-linear diffusion.

As the particles exchange energy with the waves, they are redistributed in velocity space, which in turn modifies the VDF. Because different VDF configurations excite distinct wave modes, these kinetic interactions alter the macroscopic properties of the solar wind in diverse ways.

In papers I and II, we perform a survey of Langmuir and ion-acoustic waves, respectively. These are electrostatic modes predominantly propagating parallel to the magnetic field commonly found in the solar wind and often associated with other solar wind kinetic phenomena such as MHs (Lin et al., 1996; Briand, 2015) or IP shocks (R. A. Hess et al., 1998; Wilson III et al., 2007). Despite their frequent observation, their origin, their relation to other kinetic-scale structures, and their cumulative effect on the solar wind evolution remain poorly understood.

Furthermore, in paper III, we provide a detailed analysis of the relationship between the kinetic behavior of ions across an IP shock and various waves modes, such as whistlers and ion-acoustic waves. In the following sections, we describe the properties and dispersion characteristics of the kinetic wave modes analyzed in this thesis.

### 3.1 Langmuir Waves

Langmuir waves are high-frequency electrostatic waves characterized by the following dispersion relation:

$$\omega_r^2 = \omega_{pe}^2 + 3v_{Te}^2 k^2. \quad (3.11)$$

In a Maxwellian plasma, under the weak growth approximation ( $\gamma \ll \omega_r$ ), these waves are subject to electron Landau damping, with  $\gamma$  expressed as (Treumann & Baumjohann, 1997; Gurnett & Bhattacharjee, 2017):

$$\gamma = -\sqrt{\frac{\pi}{8}} \frac{\omega_{pe}}{k^3 \lambda_{De}^3} \exp \left[ -\frac{1}{2(k\lambda_{De})^2} - \frac{3}{2} \right]. \quad (3.12)$$

This dispersion relation is plotted in Fig. 3.1b. Equations (3.11) and (3.12) are obtained by considering only the electron motion, while treating the ions as immobile. This means that we are considering perturbations with high frequencies ( $\omega_r > \omega_{pi}$ ), where the ions, due to their larger mass, cannot respond quickly enough to the rapidly oscillating fields. While ion effects exist, they can be treated as small corrections to the dispersion relation in eqs. (3.11) and (3.12).

As shown in eq. (3.11), in the limit of cold electrons,  $v_{Te} \rightarrow 0$ , the frequency reduces simply to  $\omega_{pe}$ . At this frequency, the plasma undergoes collective oscillations driven by microscopic charge separations, where the resulting electric fields provide the restoring force. When electron thermal motion is accounted for, the plasma oscillations can propagate through the medium. These

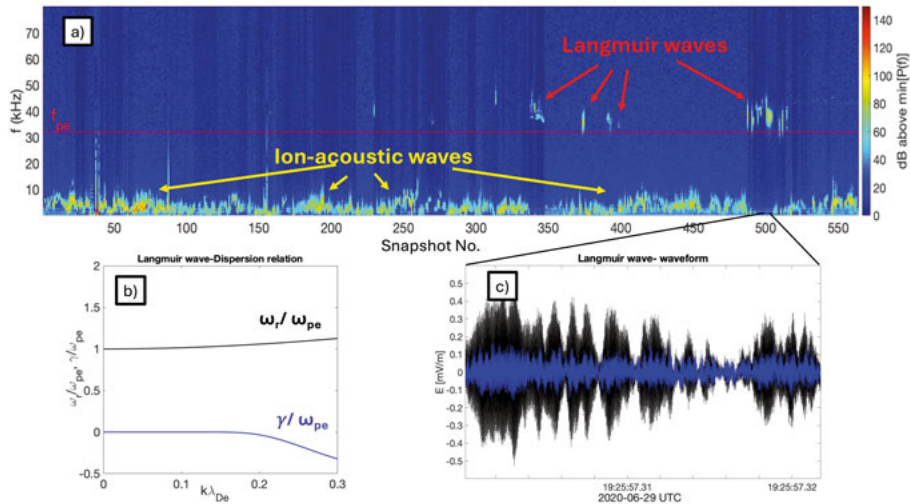


*Figure 3.1.* Langmuir waves. (a) Spectrogram of electric field waveform snapshots captured by Solar Orbiter. Several snapshots are taken every day; the x-axis indicates the snapshot number of the given day. Several Langmuir waves and ion-acoustic waves are observed on this day. (b) Dispersion relation of Langmuir waves derived from eqs. (3.11) and (3.12). At long wavelengths,  $k\lambda_{De} \ll 1$ , the frequency of Langmuir waves approaches the electron plasma frequency. (c) Electric field waveform of a Langmuir wave observed by Solar Orbiter. The wave field is mostly along the component parallel to the magnetic field,  $E_{\parallel}$  (black). The component perpendicular to the magnetic field,  $E_{\perp}$  (blue) remains near the background level.

propagating oscillations, occurring at frequencies slightly above  $\omega_{pe}$ , are the Langmuir waves.

A spectrogram of electric field waveform snapshots captured by Solar Orbiter is presented in Fig. 3.1a. Details of Solar Orbiter's snapshots are given in Chapter 4. In these observations, the Langmuir waves are identified as the narrowband emissions near the local  $f_{pe} = \omega_{pe}/2\pi$ . Moreover, these Langmuir waves are observed in the absence of radio burst signatures. An example of a Langmuir waveform is shown in Fig. 3.1c. The electric field waveform is closely aligned with the background magnetic field, as expected for Langmuir waves. Typical amplitudes for Langmuir waves in the solar wind are  $\sim 1$  mV/m, with some waves, generally the ones associated with radio burst source regions and planetary foreshocks, reaching  $\gtrsim 10$  mV/m (S. Hess et al., 2011; Briand, 2015).

Because ion dynamics play a minor role in Langmuir modes, the instabilities that trigger these waves typically originate from beam-like features in the electron VDF. This instability is called the bump-on-tail instability, where a secondary population of electrons creates a region of positive slope in  $F_{0e}$ . Figure 3.2a illustrates a typical electron VDF configuration for the bump-on-tail

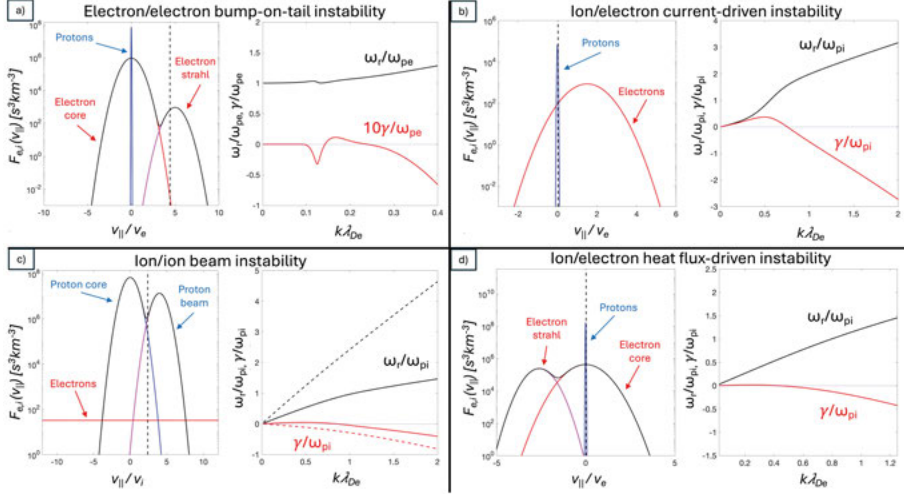


*Figure 3.2.* Four examples of the main kinetic instabilities responsible for Langmuir waves and ion-acoustic waves in the solar wind (a) Two electron population distribution unstable to the bump-on-tail instability that leads to Langmuir wave growth. (b) Electron and ion distributions unstable to the current-driven instability that leads to ion-acoustic wave growth. (c) Electron and two ion distributions unstable to the ion-beam instability that leads to ion-acoustic wave growth. (d) Ion and two electron distributions unstable to heat flux instability that leads to ion acoustic wave growth. The vertical dashed line indicates the phase velocity of the wave mode with the largest  $\gamma$ . To the right of all distributions: the corresponding dispersion relation computed numerically, displaying normalized real frequency and growth, is shown for the resulting wave modes. The dashed lines in the dispersion relation of panel (c) correspond to the damped current-driven ion-acoustic mode, resulting from the relative drift between electrons and the ion beam population.

instability alongside the corresponding dispersion relation computed numerically. For the bump-on-tail instability,  $\gamma$  depends on the density, temperature, and bulk velocity of the beam relative to the core. While the electron strahl typically does not surpass the threshold for the bump-on-tail instability (Verscharen et al., 2022; Schroeder et al., 2021), appropriate conditions may arise when the strahl interacts with other kinetic structures like MHs (Liu et al., 2025). Through Landau resonance, Langmuir waves can scatter strahl electrons into other regions of velocity space, potentially into the halo (Gary & Saito, 2007). This erodes the instability and shapes the total electron VDF. Moreover, electron beams associated with radio bursts represent a more energetic source of Langmuir waves. These beams possess drift velocities significantly higher than those of the typical strahl, resulting in much stronger wave amplitudes.

## 3.2 Ion-Acoustic Waves

For perturbations with frequencies much lower than  $\omega_{pe}$ , the response of ions becomes important. In this regime, the coupling between electron pressure and ion inertia gives rise to ion-acoustic waves. These are electrostatic modes that behave very similarly to acoustic waves in ordinary gases. The ion-acoustic mode dispersion relation is given by:

$$\omega_r = \frac{k}{(1 + k^2 \lambda_{De}^2)^{1/2}} \sqrt{\frac{(T_e + 3T_i)}{m_i}}. \quad (3.13)$$

Ion-acoustic waves are subject to both ion and electron Landau damping. In a Maxwellian plasma, under the weak growth approximation,  $\gamma \ll \omega_r$ , and assuming  $T_e \gg T_i$ , the ion-acoustic mode damping rate is expressed as (Treumann & Baumjohann, 1997; Gurnett & Bhattacharjee, 2017):

$$\gamma = -\sqrt{\frac{\pi}{8}} \frac{\omega_r}{(1 + k^2 \lambda_{De}^2)^{3/2}} \left[ \sqrt{\frac{m_e}{m_i}} + \frac{(3 + T_e/T_i)^{5/2}}{(9 + T_e/T_i)} \exp\left(-\frac{T_e}{2T_i(1 + k^2 \lambda_{De}^2)} - \frac{3}{2}\right) \right]. \quad (3.14)$$

The term inside the brackets in the top line of eq. (3.14) corresponds to the electron contribution to Landau damping, whereas the term in the bottom line corresponds to ion Landau damping, which is strongly dependent on the electron-to-ion temperature ratio  $T_e/T_i$ . The dispersion relation of ion acoustic waves is shown in Fig. 3.3 for two different values of  $T_e/T_i$ . For this dispersion relation, the ion term is of a similar form to the electron term in the Langmuir wave dispersion relation. Thus, ions behave somewhat similarly to electrons in the Langmuir mode. However, the resulting wave mode differs significantly from Langmuir waves due to the electron response. At long wavelengths,  $k\lambda_{De} \ll 1$ , these waves behave as sound waves, propagating at the ion sound speed,  $c_{ia} = \sqrt{(T_e + 3T_i)/m_i}$ , where the electrons provide the pressure gradient restoring force and the ions provide the inertia. Hence, the name ion-acoustic. It is important to bear in mind that the analytical solution in eq. (3.14) becomes less accurate at lower  $T_e/T_i$  ratios for shorter wavelengths. In these regimes, the phase velocity  $v_{ph}$  approaches  $v_{Ti}$ , leading to strong ion Landau damping that is not fully captured by the simplified analytical expression. This is shown by the blue dashed line in panel (a), where the increase of  $\gamma$  at larger  $k$  is a consequence of the analytical approximation's failure to fully account for kinetic effects. For a more precise analysis in these regimes, numerical solutions of the full kinetic dispersion relation are required.

In Fig. 3.3b, an example of an ion-acoustic wave is presented. Several ion-acoustic waves are also seen on the spectrogram in Fig. 3.1a, with frequencies

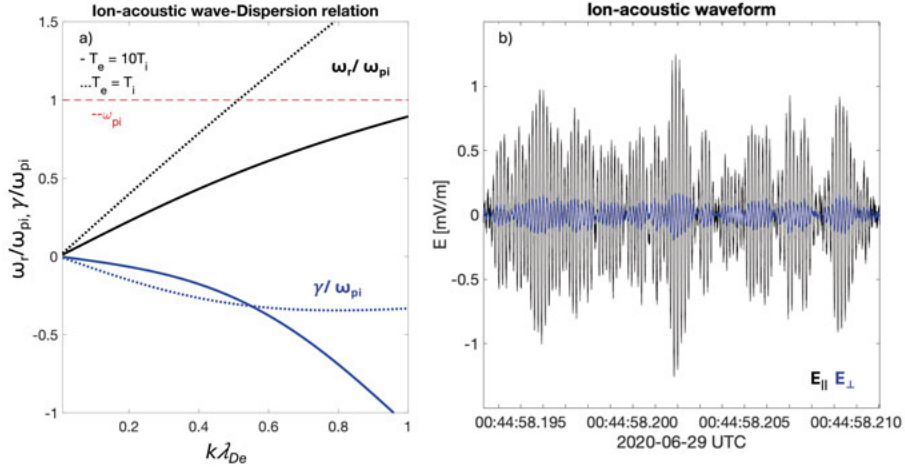


*Figure 3.3.* Ion-acoustic waves (a) Dispersion relation of ion-acoustic waves derived from eqs. (3.13) and (3.14) at two different  $T_e/T_i$  ratios. At lower  $T_e/T_i$  ratios the analytical solution in eq. (3.14) becomes less accurate for shorter wavelengths,  $k\lambda_{De} \gtrsim 1$ . (b) Waveform of an ion-acoustic wave observed by Solar Orbiter. The wave field is mostly along the component parallel to the magnetic field,  $E_{||}$  (black). The component perpendicular to the magnetic field,  $E_{\perp}$  (blue) remains near the background level.

well below  $f_{pe}$ . While the frequency of ion-acoustic waves is near  $\omega_{pi}$ , a spacecraft moving through the solar wind will observe a modified frequency due to the Doppler shift caused by the high-speed solar wind convection. In the spacecraft frame, ion-acoustic wave frequencies typically range from a few hundred Hz up to around 20 kHz (Píša et al., 2021). In contrast, because Langmuir waves occur at much higher frequencies, the relative Doppler shift they experience is almost negligible. Ion-acoustic waves are frequently observed in the solar wind (Gurnett & Anderson, 1977; Píša et al., 2021), potentially influencing the various phenomena that occur in the solar wind, such as IP shocks.

The presence of a net electric current, due to a relative drift velocity  $v_d$  between ions and electrons, can produce an instability even when both species remain individually Maxwellian. If  $v_d$  is sufficiently large, a positive slope is formed in the equivalent VDF of ions and electrons. In the plasma rest frame, this current-driven instability excites ion-acoustic waves with  $v_{ph} \approx c_{ia}$ . A typical current-driven instability VDF configuration, with corresponding dispersion relation, is presented in Fig. 3.2b. The onset of the current-driven instability depends on  $T_e/T_i$  and the drift-to-ion sound speed ratio  $v_d/c_{ia}$ . In paper II, we evaluate the current-driven instability as a potential source for the ion-acoustic waves observed near IP shocks. Our analysis demonstrates that the current-driven instability thresholds are not reached, suggesting that the

observed waves likely originate from non-Maxwellian features in the VDFs, such as proton beams or the electron strahl.

Similar to Langmuir waves, ion-acoustic waves can also be driven by a beam-like feature in the ion VDF, provided the condition in eq. (3.10) is satisfied. This is referred to as the ion-beam instability. Nonetheless, unlike Langmuir waves, the effects of both ions and electrons need to be considered. Particularly, electrons can contribute to Landau damping, so a positive slope in the ion VDF may not always lead to instability. A typical electron and ion VDF configuration for the ion-beam instability, along with the corresponding dispersion relation, is shown in Fig. 3.2c.

Finally, significant  $v_d$  can exist even in the absence of net electric currents. In the solar wind, this occurs when various plasma populations of the same particle species, typically electrons, undergo relative drifts. These drifting populations carry a heat flux acting to balance the total current. The electron heat flux in the solar wind is commonly related to non-symmetric features in the VDF along  $\mathbf{B}_0$ , such as the presence of a strahl (Treumann & Baumjohann, 1997). The heat flux-associated velocity drifts can have the same effect as current-induced velocity drifts, generating ion acoustic waves if the equivalent VDF has a positive slope. A VDF, typical for heat-flux instability onset, is shown together with its corresponding dispersion relation in Fig. 3.2d. Because the heat-flux instability involves a positive slope in the equivalent VDF and non-Maxwellian features, like beams, it is hard to disentangle it from other instabilities in spacecraft observations, causing debate regarding their role in the generation of solar wind ion-acoustic waves (Forslund, 1970; Gary, 1978; Gurnett & Frank, 1978).

### 3.3 Whistler Waves

Whistler waves are an electromagnetic mode ubiquitous in the solar wind. The frequency of this wave mode ranges from  $\omega_r > \omega_{cp}$ , where it connects with the fast magnetosonic MHD branch, up to the resonance frequency  $\omega_{ce} \cos(\theta_{kB})$ , where  $\theta_{kB}$  is the propagation angle between  $\mathbf{k}$  and  $\mathbf{B}_0$ . While the full kinetic dispersion relation of the whistler mode is quite complex, it is customary to simplify the analysis by neglecting thermal motion (i.e., cold plasma approximation) to determine the basic propagation properties. In this cold plasma approximation and for typical solar wind conditions with  $\omega_{ce} \ll \omega_{pe}$ , the dispersion relation in the whistler-mode frequency regime is given by (Baumjohann & Treumann, 1997):

$$\omega_r = \omega_{ce} \cos(\theta_{kB}) \left( \frac{k^2 c^2}{\omega_{pe}^2 + k^2 c^2} \right), \quad (3.15)$$

where  $c$  is the speed of light in vacuum. Assuming the small growth approximation ( $\gamma \ll \omega_r$ ) and frequencies below the resonance limit ( $\omega_r \ll \omega_{ce} \cos(\theta_{kB})$ ),

the collisionless damping rate due to the cyclotron harmonic number  $n = 1$  is (Treumann & Baumjohann, 1997):

$$\gamma = \frac{\sqrt{\pi}\omega_{pe}^2}{k_{\parallel}v_{Te}} \left( 2 + \frac{\omega_{pe}^2\omega_{ce}}{\omega_r(\omega_r - \omega_{ce})^2} \right)^{-1} \exp \left[ - \left( \frac{\omega_r - \omega_{ce}}{k_{\parallel}v_{Te}} \right)^2 \right]. \quad (3.16)$$

An example of a whistler-mode wave is illustrated in Fig. 3.4. Panel (b) displays the magnetic field power spectral density, showing that the observed waves are close to the lower-hybrid frequency,  $f_{lh} \approx \sqrt{f_{cp}f_{ce}}$  (where  $f_{cs} = \omega_{cs}/2\pi$ ), in the spacecraft frame. Moreover, the ellipticity shown in panel (c) indicates that these waves are right-hand polarized. While whistler-mode waves are right-handed circularly polarized in the plasma rest frame, solar wind convection can Doppler-shift their observed frequency. If the shift is sufficiently large ( $\mathbf{k} \cdot \mathbf{U} > \omega_r$ ), they appear as left-handed polarized in the spacecraft frame. Although whistler waves commonly propagate parallel to  $\mathbf{B}_0$ , oblique propagation is frequently observed (Kretzschmar et al., 2021; Colombari et al., 2024). This obliquity introduces a parallel component of the electric field ( $E_{1,\parallel} \neq 0$ ) and compressional magnetic fluctuations ( $B_{1,\parallel} \neq 0$ ), which enable the  $n = 0$  Landau and Barnes resonances to act alongside the  $n \neq 0$  cyclotron resonances already present in the case of parallel propagation. Furthermore, oblique propagation reduces the maximum frequency limit  $\omega_{ce}\cos(\theta_{kB})$ .

Because whistler-mode waves are subject to both Landau and cyclotron resonances, they can be excited by several kinetic instabilities, primarily driven by electron dynamics such as temperature anisotropies,  $T_{e,\parallel} \neq T_{e,\perp}$ , (Lazar et al., 2022), field-aligned beams (Vasko et al., 2019), or electron heat fluxes (Gary et al., 1994).

Whistler-mode waves play a central role in kinetic models of the solar wind. They have been shown to scatter the anti-Sunward strahl into the halo and subsequently into the deficit (Berčič et al., 2021a; Colombari et al., 2024). Therefore, understanding the effect of the wave-particle interactions resulting from the whistler wave generation is important for uncovering the processes involved in the diffusion of the electron deficit. This deficit, in turn, is a strong indicator of the existence of an interplanetary electric field, which contributes to the acceleration of the solar wind.

Finally, whistler-mode waves are frequently observed upstream of collisionless shocks (Wilson III, 2016; Blanco-Cano et al., 2016). These waves are typically characterized by frequencies close to  $f_{lh}$  and oblique propagation with respect to  $\mathbf{B}_0$  (Aguilar-Rodriguez et al., 2011; Ramírez Vélez et al., 2012; Kajdič et al., 2012). These whistler precursors are thought to be generated by the interaction between reflected ions and solar wind electrons through the cross-field streaming (two-stream) instability (Wu et al., 1983; Lalti et al., 2022), or radiated away from the shock ramp from dispersive effects (Kennel et al., 1985).

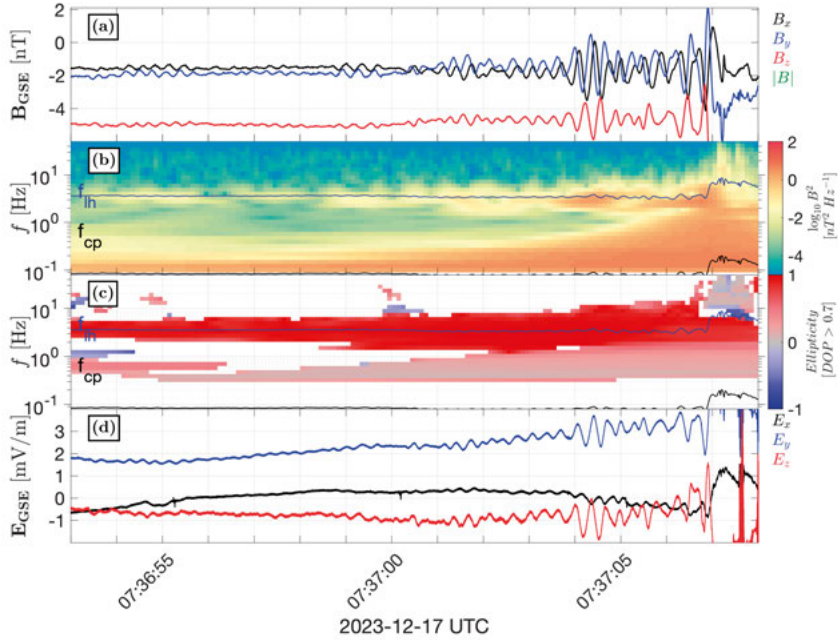


Figure 3.4. Example of a whistler-mode wave as seen by a spacecraft. (a) Magnetic field components and magnitude in Geocentric Solar Ecliptic (GSE) coordinate frame. (b) Power spectral density (PSD) of the magnetic field (c). Ellipticity of the waves, red indicates right-handed polarization and blue, left-handed polarization. (d) Magnetic field components in GSE coordinate frame. The whistler waves are more prominent at the right of this time interval. The proton cyclotron frequency ( $f_{cp}$ ) and the lower-hybrid frequency ( $f_{lh}$ ) are plotted in panels (b-c) for reference.

In paper III, we identified whistler-mode precursors at two locations of the same IP shock observed nearly simultaneously by the Magnetospheric MultiScale (MMS) spacecraft and Solar Orbiter. We analyzed their effect on the kinetic structure of the shock’s downstream region and concluded that their influence was negligible for the observed downstream magnetic oscillations. Specifically, the downstream structure of the shock exhibited distinct behavior at both locations despite the presence of the whistler precursors. However, we note that in cases where whistler precursors contribute significantly to ion bulk deceleration or heating, they could potentially play a more active role in shaping the downstream kinetic structure of low  $M_A$  IP shocks by suppressing downstream magnetic oscillations.

## 4. Solar Orbiter

To probe the solar wind using kinetic waves, we need high-resolution measurements of the electric and magnetic fields and the particles. Moreover, to investigate the impact of these waves on the evolution of the solar wind, it is necessary to monitor the solar wind across different heliocentric distances. We focus on the inner heliosphere using the Solar Orbiter mission (Müller et al., 2020).

Solar Orbiter was launched in February 2020, and since then, it has been monitoring the solar wind in the inner heliosphere. It orbits the Sun at distances ranging from 0.28 au to 1.1 au. The Solar Orbiter payload consists of six remote-sensing instruments and four in-situ experiments. The allocation of the instruments onboard Solar Orbiter is shown in Fig. 4.1. To investigate the kinetic waves in the solar wind, we utilized the Radio and Plasma Waves (RPW) instrument (Maksimovic et al., 2020). For the particle measurements, the Solar Wind Analyzer (SWA) instrument (Owen et al., 2020) was used. Magnetic field data were retrieved from the Magnetometer (MAG) instrument (Horbury et al., 2020). Solar Orbiter is also equipped with the Energetic Particle Detector (EPD) (Rodríguez-Pacheco et al., 2020), capable of detecting energetic particle fluxes with energies around a few keV up to several MeV.

### 4.1 Radio and Plasma Waves

The main source of observations analyzed in this thesis is from the RPW instrument suite. The RPW instrument is capable of detecting electric fields from  $\sim$ DC values up to tens of MHz, and is well suited to detect electrostatic waves in the solar wind. Besides the electric field, RPW also provides electron density,  $n_e$ , derived from spacecraft potential,  $V_{sc}$ , measurements. This instrument consists of a set of three antennas of 6.5 m each, located in the spacecraft's yz-plane and a three-axis search coil magnetometer (SCM) for high-resolution magnetic field, as indicated in Fig. 4.1.

The electric field measurements are processed by four different units, covering various frequency ranges. The Low Frequency Receiver (LFR) handles signals from near DC to approximately 10 kHz. The Thermal Noise Receiver (TNR) and High Frequency Receiver (HFR) focus mainly on observations of radio waves, covering frequencies ranging from 4 kHz to 16 MHz. In the middle frequencies, between 200 Hz and 200 kHz, the Time Domain Sampler (TDS) provides electric field signals in the form of high-resolution snapshots.

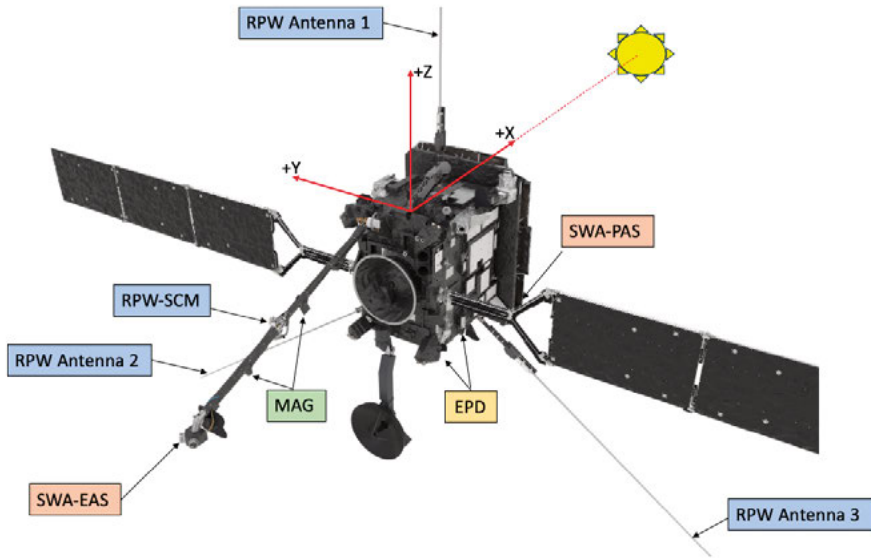


Figure 4.1. Solar Orbiter spacecraft in-situ experiments and spacecraft reference frame configuration. The x-axis points toward the Sun, the y-axis points opposite to the velocity vector, and the z-axis is perpendicular to the orbital plane, completing the right-hand triad. Adapted from <https://www.esa.int/ScienceExploration/SpaceScience/SolarOrbiter>

With solar wind Langmuir waves ranging from 20 kHz to 60 kHz (S. Hess et al., 2011; Briand, 2015) and Doppler-shifted ion-acoustic waves from a few hundred Hz to  $\sim 20$  kHz (Píša et al., 2021), TDS’s temporal resolution is sufficient to capture them. The waveform snapshots produced by TDS are typically sampled at 262.1 kHz, with a duration of  $\sim 60$  ms. The Langmuir and ion-acoustic wave snapshots shown in Figs. 3.1a,c and 3.3b, respectively, were captured by TDS. While TDS triggers snapshots at regular one-second intervals, telemetry constraints dictate that only the ones assigned the highest onboard quality flag—based on bandwidth and amplitude thresholds—are downlinked to Earth (Souček et al., 2021).

Given the telemetry constraints that prevent the transmission of all snapshot waveforms, TDS generates an onboard statistical data product (TDS-STAT). The TDS-STAT data product provides a continuous summary of wave activity by calculating parameters such as median frequency, maximum amplitude, and RMS amplitude for all snapshots identified as containing waves within a 16-second interval. Because one snapshot is processed every second, the maximum number of waves a TDS-STAT packet contains is 16. Waves are identified using a dedicated onboard detection algorithm (Souček et al., 2021). In this way, continuous data of waves are available, making the TDS-STAT product useful for statistical studies.

Finally, the Maximum Amplitude (TDS-MAMP) data product provided by TDS offers a high-resolution record of wave envelopes. The TDS-MAMP data product provides the maximum electric field for each of the measured components. The electric field is sampled at 2.0971 MHz and recorded every 7.8 ms, providing 128 samples/second. The TDS-MAMP data are valuable for tracking the evolution and occurrence of wave packets, especially those not downlinked as full waveforms, providing nearly continuous coverage of the wave environment.

## 4.2 Solar Wind Analyzer

To understand the interaction between the kinetic waves and the particles, high-resolution measurements of VDFs are of high interest. Solar Orbiter's SWA measures VDFs and calculates the moments of ions and electrons. The Proton-Alpha Sensor (SWA-PAS) is a non-mass resolving electrostatic analyzer that measures 3D ion VDFs from 200 eV to 20 keV. Generally, SWA-PAS measures a 3D VDF every 4 s, over nine elevation angles, eleven azimuthal angles, and 96 energy channels. The sampling period is reduced to one VDF every 0.25 s during burst mode acquisition intervals. While the sensor does not have a full-sky field of view, its aperture is Sunward-facing; this is sufficient for resolving the highly directional anti-Sunward ion VDFs.

In contrast, solar wind electrons necessitate a full-sky field of view to fully capture the VDF. This is achieved by the Electron Analyzer System (SWA-EAS), also part of the SWA consortium, which consists of two electrostatic analyzer sensor heads mounted on a 4.4 m boom in the shadow of the spacecraft. The cadence of EAS is nominally 4 s, and it is designed to measure electrons with energies from a few eV to  $\sim 5$  keV. The measurements from the two sensor heads are combined to generate 3D VDFs. These measurements are subsequently used to compute the distribution of particles according to the angle between the particle velocity vector and the local magnetic field. This angle, known as the pitch angle, allows for the characterization of pitch angle distributions. These types of distributions are useful for inspection of non-Maxwellian features in the VDF, for example, electron anisotropies and the electron strahl.

## 4.3 Magnetometer

Magnetic field data are available through MAG. This instrument consists of a three-axis fluxgate magnetometer mounted on the same boom as the EAS sensor heads. In its normal operation mode, MAG delivers 8 vectors per second, which increases to 64 vectors per second in burst mode. It has a dynamic range of  $\pm 128$  nT and nominal resolution of 4 pT. Magnetic field measure-

ments are essential for characterizing the solar wind conditions around regions with high wave activity. For instance, MAG data allows for the investigation of correlations between electrostatic waves and magnetic structures such as MHs. Additionally, the magnetic field vector serves as the primary reference for VDF representation. The transformation of the VDF into components parallel and perpendicular to the magnetic field is fundamental to identify features linked to kinetic instabilities, such as temperature anisotropies or heat-fluxes. Furthermore, magnetic field data enables polarization analysis of the waves, providing insight into the wave modes and propagation characteristics of the detected electromagnetic fluctuations.

## 4.4 Electron Density Estimation

The electron density  $n_e$  is a fundamental plasma property required for characterizing kinetic waves. However, investigating processes at these scales requires a much higher temporal resolution than the 4 s sampling period provided by the SWA instrument. By utilizing high-cadence  $V_{sc}$  measurements from RPW, we can derive  $n_e$  at a higher resolution, obtaining a data point every 0.0625 s in normal mode and every 0.0039 s in burst mode.

The relationship between  $V_{sc}$  and  $n_e$  is determined by the polarity of  $V_{sc}$ , which, under typical solar wind conditions, is positive. The  $V_{sc}$  is controlled by the equilibrium of electric currents flowing to and from the spacecraft conductive surface  $S$ . The main outward current is driven by the photoelectric effect, where solar UV photons remove photoelectrons from the spacecraft's sunlit surface  $S_{ph}$ . The photoelectron current  $I_{ph}$  is balanced by an inward current driven by ambient solar wind electrons collected by the spacecraft. The equilibrium value of  $V_{sc}$  therefore adjusts until the total net current is zero. Because the spacecraft charging timescale is significantly shorter than the instrument sampling period, the current balance is maintained for every measurement, enabling the derivation of  $n_e$  at high cadence.

The current balance condition of a spacecraft immersed in the solar wind is illustrated in Fig. 4.2. For a positively charged spacecraft ( $V_{sc} > 0$  V), a portion of the emitted photoelectrons is attracted back to the spacecraft's surface, effectively reducing the net  $I_{ph}$  from its maximum value, known as the photo-saturation current  $I_{ph0}$ . The energy distribution of photoelectrons is typically modeled as a Maxwellian with an empirical temperature  $T_{ph}$  of approximately 2 eV (Grard, 1973). This temperature dictates the fraction of photoelectrons with sufficient kinetic energy to overcome the spacecraft's positive potential and escape into the surrounding plasma, thus controlling  $I_{ph}$ . On the other hand, if  $V_{sc} < 0$  V, all photoelectrons escape and  $I_{ph} = I_{ph0}$ .

The solar wind electron current  $I_e$  is a function of both  $n_e$  and  $T_e$ . While other currents exist, such as those from secondary electron emission or solar wind ion collection, they are often negligible in the solar wind compared to

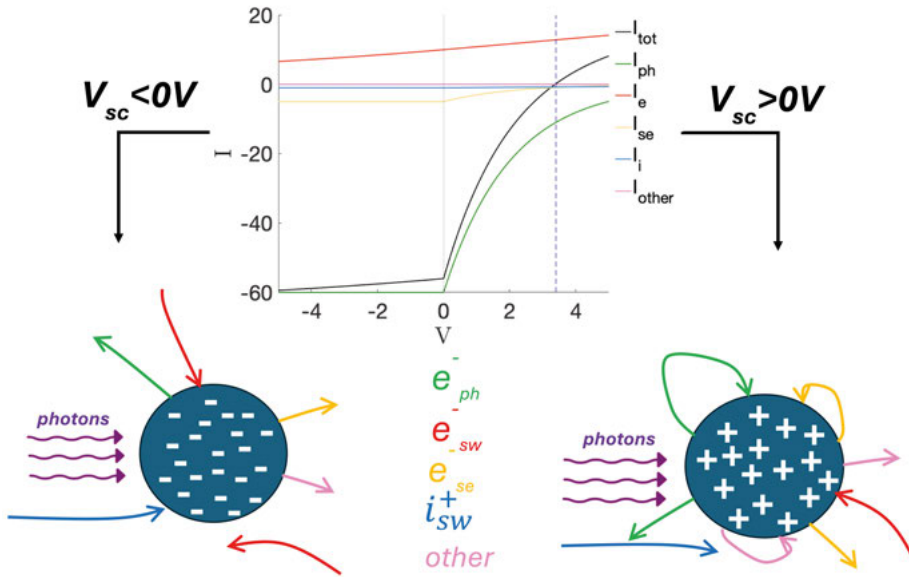


Figure 4.2. Current balance of a metallic body, such as a spacecraft, immersed in the solar wind. Different contributions to the charge transfer between the solar wind plasma and the metallic object for negative (left) and positive (right)  $V_{sc}$ . The plot in the middle depicts an example of theoretical currents as a function of  $V_{sc}$  for arbitrary parameters and spherical geometry. The black curve corresponds to the sum of all currents from and to the metallic object. The blue vertical dashed line indicates the value of  $V_{sc}$  at which the currents balance, corresponding to the spacecraft floating potential.

$I_{ph}$ . Thus, to a first approximation, the balance between  $I_{ph}$  and  $I_e$  determines the equilibrium or ‘floating’ potential  $V_{sc}$ . When  $V_{sc}$  is positive, this relation is given by (Mott-Smith & Langmuir, 1926; Pedersen et al., 2008):

$$V_{sc} = \frac{\kappa_B T_{ph}}{q} \ln \left( \frac{S_{ph}}{S} \frac{J_{ph0}}{n_e q \sqrt{\kappa_B T_e / 2\pi m_e}} \right), \quad (4.1)$$

where the photosaturation current density is given by  $J_{ph0} = I_{ph0}/S_{ph}$ . Rearranging eq. (4.1),  $n_e$  can be expressed as a function of  $V_{sc}$ . In practice, since  $T_e$  varies slowly and  $T_{ph}$  is typically constant, the terms can be grouped into two calibration parameters,  $n_0$  and  $\beta$ . Using the measured probe-to-spacecraft potential  $-V_{ps}$  as a proxy for  $V_{sc}$ , the following simplified relationship is obtained:

$$n_e = n_0 e^{V_{ps}/\beta}, \quad (4.2)$$

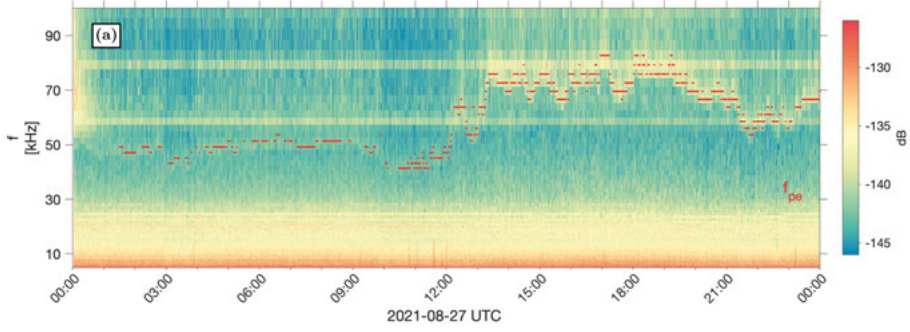


Figure 4.3. Example of TNR measurements. (a) Dynamic spectra of the antenna 1 - antenna 2 voltage signal. The plasma line, corresponding to  $f_{pe}$ , is visible as the enhanced signal between  $\sim 50$ -80 kHz. The red dots correspond to the low-cadence, non-continuous reference  $n_e$ .

where the calibration parameters are theoretically defined by:

$$n_0 = \frac{S_{ph}}{S} \frac{J_{ph0}}{q \sqrt{\kappa_B T_e / 2\pi m_e}} \quad \text{and} \quad \beta = \kappa_B T_{ph} / q. \quad (4.3)$$

Rewriting  $n_e$  this way allows for a standard linear regression in log-linear space to determine  $n_0$  and  $\beta$  empirically. The linear regression is performed using a reference  $n_e$  derived from a semi-automated  $f_{pe}$  detection routine applied to the TNR spectra. An example of the reference  $n_e$  retrieved from TNR spectra is shown in Fig. 4.3. The red dots correspond to the retrieved reference  $n_e = (f_{pe}/8.980)^2$ , where  $n_e$  is in  $\text{cm}^{-3}$  and  $f_{pe}$  in kHz. This semi-automated detection provides a reliable density  $n_e$  reference but is constrained by on-board interference, finite frequency resolution, and periods where  $f_{pe}$  (i.e., the plasma line) is not clearly identifiable. Consequently, the TNR-derived  $n_e$  is discontinuous and has a low time resolution (4–16 s). However, by fitting the reference  $n_e$  data points over specific time intervals, the high-cadence  $V_{ps}$  measurements are converted into a continuous, high-resolution  $n_e$  time series.

This method has been employed in previous missions, such as GEOTAIL (Nakagawa et al., 2000), Polar (Laakso et al., 2002), Cluster (Pedersen et al., 2008), and Parker Solar Probe (Mozer et al., 2022). While it provided reliable results during the early stages of the Solar Orbiter mission (Khotyaintsev et al., 2021), a change in the  $V_{sc} - n_e$  relationship was observed approximately one year after launch. Specifically, it evolved from a single exponential to a two-exponential relation. This transition occurs because  $V_{sc}$  began to reach negative values in certain plasma environments. We identified the primary cause of the drop in measured  $V_{sc}$  to be the electrical disconnection of the solar panels from the spacecraft's common ground. This disconnection significantly reduced the ratio of sunlit area to the total conductive area,  $S_{ph}/S$ , which results in a lower  $V_{sc}$ . As discussed, a negative  $V_{sc}$  alters the current

balance by allowing all photoelectrons to escape while increasingly repelling the ambient solar wind electrons. Rewriting the expression for  $V_{sc}$  with  $n_e$  for negative potential yields:

$$V_{sc} = \frac{\kappa_B T_e}{q} \ln \left( \frac{S_{ph}}{S} \frac{J_{ph0}}{n_e q \sqrt{\kappa_B T_e / 2\pi m_e}} \right). \quad (4.4)$$

The main difference between eqs. (4.1) and (4.4) is the dependence on  $T_e$  rather than  $T_{ph}$ . This modifies the calibration parameter  $\beta$  as:

$$\beta = \kappa_B T_e / q. \quad (4.5)$$

By accounting for both  $V_{sc}$  polarities, we derive unique calibration parameters for different plasma environments. This approach allows for the estimation of  $n_e$  at all times when  $V_{ps}$  measurements are available, providing the high-resolution  $n_e$  required for our analysis. This methodology, described in further detail in paper IV, has been used to deliver continuous  $n_e$  data since 2021, including the data used for the analyses in papers I, II, and III.

## 5. Summary of Publications

### 5.1 *Paper I: Langmuir Waves Associated with Magnetic Holes in the Solar Wind*

**J. J. Boldú**, D. B. Graham, M. Morooka, M. André, Yu. V. Khotyaintsev, T. Karlsson, J. Souček, D. Píša and M. Maksimovic.  
Astronomy and Astrophysics (2023). Volume 674, Solar Orbiter First Results (Nominal Mission Phase)  
doi: 10.1051/0004-6361/202346100.

In this study, we investigate the occurrence and properties of Langmuir waves in the solar wind across different heliocentric distances. By categorizing these waves based on their association with radio burst source regions, we found that the majority (73%) of Langmuir waves are actually unrelated to radio bursts. Approximately 80% of the non-radio burst Langmuir waves occurred when the local magnetic field was below background levels, with 8% found in deep magnetic holes where the field strength dropped by more than 50%.

Nevertheless, our findings suggest that a magnetic hole by itself is insufficient to trigger Langmuir wave activity, as many holes were observed without associated waves. A detailed analysis of two magnetic hole observations revealed that enhanced Langmuir wave activity occurred when an electron strahl was also present. This suggests that the interaction between this electron population and magnetic depressions is likely a necessary condition for Langmuir wave generation. Finally, we note that non-radio burst Langmuir waves typically exhibit amplitudes below 1 mV/m, making them significantly weaker than the high-amplitude waves found in radio burst source regions. These results suggest that magnetic holes could be important regions for electron VDF evolution and strahl scattering, providing evidence for a potential link between electron-scale kinetic processes (Langmuir waves) and ion-scale structures (Magnetic holes).

**My contribution:** I performed the data analysis and had the main responsibility of writing the paper.

## 5.2 *Paper II: Ion-acoustic Waves Associated with Interplanetary Shocks*

J. J. Boldú , D. B. Graham , M. Morooka, M. André , Yu. V. Khotyaintsev , A. Dimmock, D. Příša, J. Souček , M. Maksimovic, P. Louarn , A. Fedorov, G. Nicolaou , and C. J. Owen.

Geophysical Research Letters (2024), 51, e2024GL109956.

doi:10.1029/2024GL109956

We investigate the occurrence rate of ion-acoustic waves found in the vicinity of IP shocks, comparing it to the occurrence rate of the waves observed in the ambient solar wind. Using a dataset of 80 IP shocks observed by Solar Orbiter across different heliocentric distances, we find that ion-acoustic wave occurrence rate near IP shocks is almost three orders of magnitude higher than in the ambient solar wind, with the rates increasing with decreasing distance to the ramp.

In the upstream region, the ion-acoustic wave occurrence rate increases at smaller heliocentric distances and remains above ambient solar wind levels for significantly extended upstream distances from the shock. Notably, we found no clear correlation between shock parameters and ion-acoustic wave occurrence rate. While these waves often coincide with enhanced currents, our analysis indicates that such currents are insufficient to trigger ion-acoustic wave growth under standard Maxwellian VDFs.

Detailed case studies of two IP shocks revealed that enhanced upstream ion-acoustic wave activity occurred alongside an ion-beam and electron strahl. In contrast, when such non-Maxwellian features were absent, reduced wave activity was observed. This suggests that the excitation of ion-acoustic waves is driven by non-Maxwellian proton and electron distributions, likely via ion-beam or heat-flux kinetic instabilities.

Furthermore, the downstream region exhibits more variable wave activity between IP shocks, and in general, it decreases rapidly with distance from the ramp. This indicates that downstream ion-acoustic waves are more intrinsically linked to local shock dynamics than those in the extended upstream region.

**My contribution:** I performed the data analysis and had the main responsibility of writing the paper.

### 5.3 *Paper III: Kinetic Structure of an Interplanetary Shock Observed at Two Heliocentric Longitudes*

**J.J. Boldú**, D. B. Graham, M. Morooka, M. André, Yu. V. Khotyaintsev, A. Dimmock, A. Lalti, D. Příša, J. Souček, M. Maksimovic, P. Louarn, A. Fedorov and C. J. Owen.

Under review in Journal of Geophysical Research: Space Physics.

In this study, we analyze two crossings of the same IP shock observed by Solar Orbiter and the Magnetospheric MultiScale (MMS) spacecraft. The observations were taken while both spacecraft were at similar heliocentric distances, but separated in heliographic longitude. This multi-spacecraft configuration, combined with high-resolution kinetic measurements from MMS, allowed for a detailed investigation into how ion-scale processes shape the IP shock profile.

At both locations, the shock exhibited similar macro-scale properties, characterized by a low  $M_A$  ( $\sim 2-3$ ) and oblique geometry ( $\theta_{Bn} \sim 67^\circ - 70^\circ$ ). Both spacecraft also detected whistler wave precursors upstream of the ramp.

Despite these similarities, the shock kinetic structure differed significantly between the two longitudes observed. In particular, MMS resolved low-frequency compressional downstream magnetic oscillations, coupled with intermittent ion-acoustic wave activity that matched the periodicity of the downstream magnetic oscillations. In contrast, the downstream magnetic oscillations are absent, and the ion-acoustic wave activity is significantly reduced at the Solar Orbiter location.

By comparing the ion VDF measurements with a test-particle model, we found that ion behavior across the IP shock manifests significantly differently between the two spacecraft locations. At the MMS location, we identified reflected protons and, for the first time, reflected  $\alpha$ -particles at an IP shock.

The data reveal that the downstream magnetic oscillations are driven by VDF fluctuations. We hypothesize that these same VDF fluctuations alter kinetic instability thresholds, triggering the intermittent ion-acoustic waves. This suggests a direct relation between downstream magnetic oscillations and ion-acoustic waves.

The absence of the downstream magnetic oscillations at Solar Orbiter is likely due to a combination of a lower magnetic compression ratio and a smaller upstream normal velocity. This smaller velocity is partly a result of the non-radial shock-normal direction at Solar Orbiter. Particularly, our results demonstrate that the kinetic behavior of ions across IP shocks is highly sensitive to relatively small variations in upstream parameters. These findings provide compelling evidence of how kinetic processes and local geometry shape the evolution of solar wind structures, such as IP shocks.

**My contribution:** I performed the data analysis and had the main responsibility of writing the paper.

## 5.4 *Paper IV: Electron Density Estimation from Spacecraft Potential Measurements using Solar Orbiter*

**J.J. Boldú**, D. B. Graham, Yu. V. Khotyaintsev, M. Morooka, A. Eriksson, M. André, M. Maksimovic, A. Vecchio, G. Nicolaou, S. Štverák, C. J. Owen, and C. Watson.

Submitted to *Astronomy and Astrophysics*.

Analyzing solar wind processes at kinetic scales requires high-resolution electron density measurements. Onboard Solar Orbiter, these are typically derived from the spacecraft potential; however, the spacecraft's complex electrostatic environment and disturbances from the solar panels required a revisit of the existing density estimation method. This article details the refinement of the RPW density calibration to ensure data reliability across diverse plasma and spacecraft conditions.

A primary challenge we identified was the occurrence of extended periods where  $V_{sc}$  became negative. This behavior first appeared following discrete events that left the solar panels electrically disconnected from the spacecraft ground, creating a more complex relationship between  $n_e$  and  $V_{sc}$  than previously modeled. To address this, we modified the density calibration to account for negative  $V_{sc}$ , allowing for the delivery of high-resolution data regardless of the polarity of  $V_{sc}$ .

We also analyzed the physical significance of the calibration parameters to provide indirect estimates of photoelectron and solar wind electron temperatures. We obtained a mean  $T_{ph}$  of 2 eV, which aligns well with experimental values. Furthermore, after correcting for solar panel effects, our  $T_e$  estimates showed strong agreement with independent measurements from SWA-EAS.

The calibrated datasets were utilized in the research presented in Papers I-III, and have become a resource for the broader heliophysics community. These data have supported various solar wind studies, including radio bursts, IP shocks, mirror-mode storms, magnetic holes, and Venus-induced magnetosphere.

**My contribution:** I performed the data analysis, data calibration, and had the main responsibility of writing the paper.

## 6. Reflections and Outlook

The research presented in this thesis represents a contribution toward an understanding of the solar wind evolution. It builds upon foundational work in heliospheric physics, which established that non-LTE VDFs dominate solar wind dynamics. The subsequent discovery of the ubiquity of plasma waves provided crucial evidence on the nature of a solar wind driven by wave-particle interactions. After these previous findings, our work has focused on characterizing and quantifying the presence of relevant kinetic wave modes in the solar wind, linking them to specific plasma structures across various scales. However, these results also uncover several open questions that remain to be addressed in future research.

### **Energy Densities and Global Energetics**

With missions like Solar Orbiter continuously monitoring the solar wind across different heliocentric distances, extensive databases of kinetic wave modes have been compiled, including Langmuir (Graham et al., 2021, paper I), ion-acoustic (Píša et al., 2021, paper II), whistlers (Kretzschmar et al., 2021), and ion-cyclotron waves (Carbone et al., 2021). A natural continuation of these works is to quantify the cumulative contribution of each of these wave modes to the solar wind energy budget as it expands through the heliosphere. Specifically, determining the proportion of energy being transferred from kinetic waves into the plasma—and identifying the heliocentric distances and solar wind regimes where this process is dominant—is essential for quantifying the global impact of wave-particle interaction on solar wind energetics.

Furthermore, characterizing these energy densities will provide insight into the constraints imposed by kinetic instabilities to prevent further deviations from non-LTE. This could clarify the regulation of various sources of free energy, such as strahl velocity and density, drifts between particle species, and temperature anisotropies. Understanding the restriction imposed on deviations from equilibrium by kinetic waves may also provide insight into the VDF closer to the Sun, offering clues about the primary mechanisms of solar wind acceleration.

### **The Origin of Kinetic Instabilities**

An outstanding question remains regarding the origin of the kinetic waves in the solar wind. Precisely identifying the instabilities responsible for wave emission is necessary to understand how waves act upon VDFs to drive them

toward stable configurations. To accomplish this, future missions must incorporate measurements that resolve electron-scale processes throughout the heliosphere.

For example, while ion-acoustic waves are frequently observed alongside ion beams (Gurnett & Frank, 1978), conclusive evidence that ion-beam instabilities are the primary drivers remains elusive. Furthermore, the potential influence of the electron strahl on the instability thresholds and dispersion properties of these waves is not yet fully understood. Identifying these wave dispersion properties will require full 3D electric field vector measurements obtained under conditions of electromagnetic cleanliness. Additionally, continuous coverage across varying heliocentric distances is essential; however, such high-cadence data remains currently limited by restrictive telemetry budgets. Nonetheless, determining the origin of these waves has significant implications; in the case of ion beams, it could explain the observed evolution of beam characteristics as a function of heliocentric distances.

Moreover, the generation of Langmuir waves within MHs provides a unique opportunity to study the coupling between electron-scale and ion-scale processes. While current hypotheses focus on the presence of an electron strahl component as a source of free energy (Liu et al., 2025), their role requires observational validation. Although high-resolution electron measurements are often limited in the inner heliosphere, Earth-orbiting spacecraft such as MMS, which regularly probes the solar wind, can provide the high-cadence data necessary to definitely evidence these generation mechanisms.

Finally, recent observations of whistler waves indicate simultaneous detection of Langmuir waves, suggesting a potential connection between their generation mechanisms (Jagarlamudi et al., 2021). Investigating this relationship will provide insights into the interplay that occurs at different scales, specifically how the free-energy source that excites one wave mode might simultaneously favor or trigger another. Generally, the overall result of these multi-scale interactions is a reconfiguration of the VDFs. These effects on the VDFs must be further investigated to understand their relevance in the global evolution of the solar wind.

### **Kinetic Processes at Interplanetary Shocks**

Kinetic waves are thought to play a dominant role in sustaining collisionless shocks, yet quantitative evidence regarding their contribution to dissipation in IP shocks remains scarce (Wilson III et al., 2007). The impact of these waves across a broader range of shock parameters and heliocentric distances requires further investigation as well. Quantifying how modes like ion-acoustic waves contribute to energy dissipation at IP shocks is a vital step in understanding fundamental collisionless plasma physics. Efforts have been made to resolve these questions; for instance, new onboard detection algorithms for IP shocks have been developed for Solar Orbiter, which permit the transmission of continuous high-frequency electric field snapshots and  $V_{sc}$  measurements up to

a sampling frequency of 4096 kHz. With these high-resolution data, it will be possible to perform a more in-depth analysis of energy dissipation at IP shocks.

New Solar Orbiter IP shock observations reveal that the ion dynamics leading to the downstream magnetic oscillations observed in paper III, may be a more common process in low- $M_A$  shocks than previously thought and potentially could be present in higher  $M_A$  regimes as well. A statistical analysis of this phenomenon would provide key insights into the ion behavior that shapes observed magnetic profiles and contributes to the thermalization of ion VDFs. Furthermore, as we demonstrate, the kinetic behavior of different ion species manifests in distinct ways during shock encounters. Consequently, mass-resolving instrumentation is a requirement for future missions to successfully distinguish proton behavior from heavier ion contributions, in particular  $\alpha$ -particles.

Future work should also address the kinetic instabilities that potentially arise from the VDF fluctuations downstream of IP shocks. Disentangling the roles of these VDF fluctuations from proton-alpha drifts, reflected proton beams, and the electron strahl in generating the ion-acoustic waves will clarify how VDFs respond to shocks through kinetic-scale processes.

### **Implications for Solar Wind Heating and Acceleration**

Due to deviations from LTE, the macroscopic properties of the solar wind differ significantly from predictions of simple adiabatic expansion. However, when these deviations become sufficiently large, kinetic instabilities arise, preventing the deviations from further increasing. Identifying which specific wave modes regulate which non-equilibrium features is imperative for explaining observed solar wind properties. Ultimately, any theory proposing a mechanism for solar wind acceleration near the Sun must remain consistent with the observed evolution of the plasma further out in the heliosphere. With a clearer understanding of wave occurrence, source regions, and radial distribution now established, the next logical step is to quantify their macroscopic effects on the solar wind's expansion.

A central question in kinetic solar wind physics is how the electron halo is formed and how the deficit is populated. The prevailing theory suggests that kinetic instabilities regulate these specific VDF features. Understanding the evolution of these instabilities may provide crucial insights into the nature of the electron deficit. This electron VDF feature is a key component in determining the interplanetary electric field, which ultimately contributes to the solar wind acceleration.

## 7. Sammanfattning på Svenska

Solvinden är en kontinuerlig ström av laddade partiklar och magnetfält som kommer från solens korona. Denna vind fyller solsystemet och skapar heliosfären. Heliosfärens globala dynamik beskrivs vanligtvis med magnetohydrodynamiska (MHD) modeller. Många av solvindens observerade egenskaper, såsom temperatur- och hastighetsprofiler, kan dock inte helt beskrivas med MHD-ekvationer. I solvinden med låg densitet och hög temperatur är kollisioner mellan partiklar sällsynta. Solvinden är alltså ett plasma med få kollisioner som ofta avviker från lokal termisk jämvikt (Local Thermodynamic Equilibrium, LTE). Detta visar sig som bland annat genom att elektronernas fördelningar i hastighetsrummet (Velocity Distribution Functions, VDFs) inte är Maxwellfördelningar.

Dessa avvikelser från LTE begränsas av kinetiska instabiliteter, som genererar kinetiska vågor vilka hindrar alltför stora avvikelser från Maxwell-fördelningar. Dessa vågor omfördelar energi och driver plasmat mot mer stabila fördelningar. Eftersom dessa processer sker på skalor där MHD-ekvationer inte längre är giltiga krävs en kinetisk teori. I denna avhandling använder vi data från Solar Orbiter-projektet för att undersöka hur kinetiska vågor som uppstår från instabila VDF:er påverkar solvindens utveckling.

Vi identifierar och karakteriserar flera kinetiska vågmoder som är avgörande för solvindens utveckling, och fastställer hur ofta dessa förekommer och hur de varierar med avstånd från solen. Vi fokuserar främst på elektrostatiska vågmoder och bestämmer deras samband med transienta fenomen i solvinden som kan vara viktiga för att generera vågorna, som magnetiska håll, interplanetära (IP) chocker och kortvariga utbrott på radiofrekvenser.

Vår forskning som presenteras i artikel I visar att Langmuir-vågor främst exciteras i lokaliserade magnetfältsmåner. Vi finner att mer än 70% av Langmuir vågorna i solvinden inte exciteras i samband med transienta utbrott på radiofrekvenser; dock har sådana Langmuir vågor vanligtvis högre amplitud. Dessutom fastställer vi att magnetiska håll ensamma är otillräckliga för att excitera Langmuir vågor, och att en suprathermisk elektronpopulation måste vara involverad i genereringen av vågorna.

Den andra typen av kinetisk våg vi undersöker är den jonakustiska moden. Vi fokuserar på deras förekomst nära IP-chocker och finner att jonakustisk aktivitet förstärks vid rampen av dessa chocker. Vi visar att de observerade elektriska strömmarna är otillräckliga för att starta instabiliteter som exciterar jonakustiska vågor. Istället kopplar vi dessa vågor till avvikelser från Maxwell-fördelningar hos både elektroner och joner. Specifikt handlar det om jonstrålar och hos elektroner det så kallade strahl.

I artikel III analyserar vi i detalj den kinetiska strukturen hos en IP-chock. Vi karakteriserar de vågor som är associerade med chocken. Detta inkluderar visslarvågor, jonakustiska vågor och nedströms magnetiska oscillationer. Genom att jämföra observationerna med en testpartikelmodell förklarar vi närvaron av nedströms magnetiska oscillationer med protonernas kinetiska beteende. När protoner korsar chocken blir deras gyrorörelse mer uttalad, vilket resulterar i oscillationer i VDF-momenten. Vi identifierade protonernas dynamiska tryck som den dominerande fluktuerande komponenten av det totala plasmatrycket, vilket genom tryckbalans producerar magnetiska oscillationer nedströms. Vi noterar att dessa oscillationer på jonskala är kopplade till jonakustisk vågaktivitet på elektronskala som uppstår tillfälligt med intervall som matchar periodiciteten hos de magnetiska oscillationerna nedströms.

Slutligen, för att analysera de olika kinetiska vågmoderna, utvecklade vi en förbättrad metod för att med hög upplösning uppskatta elektrondensitet från mätningar av rymdfarkostens potential  $V_{sc}$ . Denna metod beskrivs i detalj i artikel IV, där vi analyserar den elektrostatiska miljön kring rymdfarkosten Solar Orbiter. Vi undersöker störningarna som orsakas av solpanelerna, vilket gör det möjligt att identifiera förändringar i  $V_{sc}$  och sedan förbättra densitetsuppskattningen. Med denna förbättrade metod levererar vi högupplöst elektrondensitet tillgänglig för alla forskare inom heliosfärfysik.

## 8. Acknowledgements

First and foremost, I thank God for the many blessings I received during my Ph.D. years. I have been given so much, and I am grateful for the exemplary people He placed in my life to guide me. In an effort to give back what I have received, the least I can do is share the knowledge I have acquired throughout these years. I dedicate the following reflections to each of you who made it possible for me to get this far in my Ph.D.:

- **To my supervisor, Daniel:** *"Magnetic holes alone are not sufficient to trigger Langmuir waves; an external component, like the strahl, is needed".* Without your guidance and expertise acting as the essential 'external component', I certainly would have not triggered the conclusion of my Ph.D. However, unlike a transient magnetic hole, your support has been constant. Thank you for your great patience and for sharing your immense knowledge with me throughout these years. Being your student has been an honor and a truly exciting journey.
- **To my co-supervisors—Michiko, Mats and Yuri:** *"The occurrence rate of solar wind ion-acoustic waves increases near IP shocks and peaks at the ramp region".* The occurrence rate of my success has certainly increased by being surrounded by your peak minds. With your support, I have grown as a professional and as a person.
- **To my IRF colleagues:** *"Ion-acoustic waves occur in bursts matching the period of downstream magnetic oscillations".* Things that appear unrelated often end up being deeply connected. During my time at IRF, many of you have become part of my life—sometimes through intense bursts of friendship, and other times through lower-frequency moments we spent together. One way or another, you have all become an essential part of my downstream life, now that I am exiting the shock.
- **To my Ph.D. fellows—Atlas, Apopo, Alice, Jack White and Iñaki:** *"If you observe a solar wind Langmuir wave, it is likely that you are in a magnetic field depression".* If it weren't for you, I would have spent these years lost in 'depressions' and surrounded by too many Langmuir waves. You truly make me see the density enhancement within every magnetic hole.

- **To my ex-Ph.D. fellows—Josh, Ida, Ahmad, Louis, Konrad and Katerina:** *"The macroscopic structure of IP shocks is altered by the kinetic behavior of ions, which is highly sensitive to small upstream variations"*. If it weren't for the great people 'upstream' of me, my own macroscopic development would have remained stagnant; consequently, I would not have learned nearly as much. Your kindness and patience in sharing your expertise with those less experienced (like me) has made it possible for me to get this far.
- **To my friend, Kim:** *"Using the relationship between  $n_e$  and  $V_{sc}$ , we can infer indirectly other plasma parameters such as  $T_e$  and  $T_{ph}$ "*. Our relationship has not always been a perfect fit, but when we have been able to identify our polarities, it has yielded very good results. From this relationship, I have been able to obtain parameters of myself that I didn't even know I could get. Thanks for keeping my potential up!
- **To my community at the Heliga Familjens Katolska Församling:** *"There is no clear co-relation between ion-acoustic wave occurrence rate and IP shock parameters, but upstream ion-acoustic activity is enhanced closer to the Sun"*. While there were times when the path to this Ph.D. seemed to have no clear relation to anything, it is clear that the love I found here—where I drew closer to God—has been incredibly enhanced by my brothers and sisters. Without your love, I certainly would have quit long ago.
- **To my Dad:** *"An IP shock has different signatures at distinct locations"*. While my life here in Sweden has a very different signature than my life back in Mexico, your love has remained 'shockingly' amazing. Thank you for always believing in me; even when you didn't have in-situ measurements of my daily endeavors, you kept trusting your models of who I am. I am sure they have been excellent approximations.
- **To my Mom:** *"More than 70% of the solar wind Langmuir waves are not related to radio bursts"*. Sometimes my vision has been obscured by intense bursts of life, preventing me from seeing the constant love you give me. But I am certain that without your love, my strahl would not have been able to erase my deficit. Thank you for everything. Even if I do not always send Extraordinary—or even Ordinary—emissions of love, please know that it is always there, steady in the background solar wind.
- **To my siblings, Jaume and Macarena:** *"The solar panels affect the  $V_{sc}$  measurements onboard Solar Orbiter"*. Sometimes the very thing that gives you power also affects your senses; be sure to understand your

own power sources. You might not realize it, but you have influenced my entire life, I wouldn't be who I am today without your interference. And although I don't always understand you, you are the power source that keep me orbiting.

- **To my Yayos and family in Mexico:** *"Ion beams and ion-acoustic waves are often seen together upstream of IP shocks"*. I know I can always count on you whenever I am about to cross the sudden and abrupt changes in life. The definitive evidence might be elusive, but I am certain that whenever my activity is enhanced, it is because you are beaming for me.
- **To Göran, Linnéa, Agnes and Poppi:** *"Fluctuations in dynamic pressure, produced by proton gyration, are responsible for downstream magnetic oscillations"*. Life can exert a lot of pressure, but always remember that it is you who have the strength to gyrate things around and regulate any oscillation. In my own case, without you I wouldn't be able to balance all that pressure. Thanks for making my life so much better, from the scales below  $\lambda_{De}$  in the core of the Sun to beyond  $\lambda_{mfP}$  in the intergalactic medium.

Additionally, I want to thank all of you once more for making me realize that I had many interesting results to draw quotes from.

If for some reason you are still reading this far, you might be thinking that there is someone special that I haven't mentioned. The reason is that I cannot simply "thank" Myriam; she is as much an author of this thesis as I am, if not more. Because a Ph.D. goes far beyond the books, the code, the meetings, and the conferences. It also requires resolving everything outside the office walls after going home, and Myriam has been the co-author of that part of this Ph.D. My name might be on the cover of this thesis—perhaps because its catchier, or maybe no one would dare to put their name together with that cover image—but you should know that this is also her work.

# References

- Aguilar-Rodriguez, E., Blanco-Cano, X., Russell, C. T., Luhmann, J. G., Jian, L. K., & Ramírez Vélez, J. C. (2011). Dual Observations of Interplanetary Shocks Associated with Stream Interaction Regions. *Journal of Geophysical Research: Space Physics*, 116(A12), A12109. doi: 10.1029/2011JA016559
- Akimoto, K., & Winske, D. (1989). Nonlinear Generation of Whistler Waves by an Ion Beam. *Journal of Geophysical Research: Space Physics*, 94(A12), 17259–17265. doi: 10.1029/JA094iA12p17259
- Alexandrova, O., Saur, J., Lacombe, C., Mangeney, A., Mitchell, J., Schwartz, S. J., & Robert, P. (2009). Universality of Solar-wind Turbulent Spectrum from MHD to Electron Scales. *Physical review letters*, 103(16), 165003. doi: 10.1103/PhysRevLett.103.165003
- Alfvén, H. (1942). Existence of Electromagnetic-hydrodynamic Waves. *Nature*, 150(3805), 405–406. doi: 10.1038/150405d0
- Baby, J. A. (2023). *Evolution of Solar Wind Electrons in the Inner Heliosphere* (Unpublished doctoral dissertation). UCL (University College London).
- Baby, J. A., Owen, C. J., Verscharen, D., Bakrania, M., Stansby, D., Wicks, R. T., ... others (2022). Radial Evolution of Thermal and Suprathermal Electron Populations in the Slow Solar Wind from 0.13 to 0.5 au: Parker Solar Probe Observations. *The Astrophysical Journal*, 931(2), 118. doi: 10.3847/1538-4365/ab4cec
- Badman, S. T., Stevens, M. L., Bale, S. D., Rivera, Y. J., Klein, K. G., Niembro, T., ... others (2025). Multispacecraft Measurements of the Evolving Geometry of the Solar Alfvén Surface over Half a Solar Cycle. *The Astrophysical Journal Letters*, 995(2), L37. doi: 10.3847/2041-8213/ae0e5c
- Balikhin, M. A., Zhang, T. L., Gedalin, M., Ganushkina, N. Y., & Pope, S. A. (2008). Venus Express Observes a New Type of Shock with Pure Kinematic Relaxation. *Geophysical Research Letters*, 35. doi: 10.1029/2007GL032495
- Balogh, A., & Treumann, R. A. (2013). *Physics of Collisionless Shocks: Space Plasma Shock Waves*. Springer Science & Business Media.
- Barnes, A. (1992). Acceleration of the Solar Wind. *Reviews of Geophysics*, 30(1), 43–55. doi: 10.1029/91RG02816
- Baumjohann, W., & Treumann. (1997). *Basic Space Plasma Physics* (First ed.). Imperlai College Press.
- Bellan, P. M. (2008). *Fundamentals of Plasma Physics*. Cambridge university press.
- Berčić, L., Maksimovic, M., Halekas, J. S., Landi, S., Owen, C. J., Verscharen, D., ... others (2021b). Ambipolar Electric Field and Potential in the Solar Wind Estimated from Electron Velocity Distribution Functions. *The Astrophysical Journal*, 921(1), 83. doi: 10.3847/1538-4357/ac1f1c
- Berčić, L., Verscharen, D., Owen, C. J., Colomban, L., Kretzschmar, M., Chust, T., ... others (2021a). Whistler Instability Driven by the Sunward Electron Deficit in

- the Solar Wind. High-cadence Solar Orbiter Observations. *Astronomy & Astrophysics*, 656, A31. doi: 10.1051/0004-6361/202140970
- Biermann, L. (1951). Kometenschweife und Solare Korpuskularstrahlung. *Zeitschrift für Astrophysik*, Vol. 29, p. 274, 29, 274.
- Birkeland, K. (1914). A possible Connection Between Magnetic and Meteorologic Phenomena. *Monthly Weather Review*, 42(4), 211–211.
- Blanco-Cano, X., Kajdič, P., Aguilar-Rodríguez, E., Russell, C., Jian, L., & Luhmann, J. (2016). Interplanetary Shocks and Foreshocks Observed by STEREO During 2007–2010. *Journal of Geophysical Research: Space Physics*, 121(2), 992–1008. doi: 10.1002/2015JA021645
- Briand, C. (2009). Plasma Waves Above the Ion Cyclotron Frequency in the Solar Wind: A Review on Observations. *Nonlinear Processes in Geophysics*, 16(2), 319–329. doi: 10.5194/npg-16-319-2009
- Briand, C. (2015). Langmuir Waves Across the Heliosphere. *Journal of Plasma Physics*, 81(2), 325810204. doi: 10.1017/S0022377815000112
- Briand, C., Soucek, J., Henri, P., & Mangeney, A. (2010). Waves at the Electron Plasma Frequency Associated with Solar Wind Magnetic Holes: STEREO/Cluster Observations. *Journal of Geophysical Research: Space Physics*, 115(A12). doi: 10.1029/2010JA015849
- Cairns, I. H., Knock, S., Robinson, P., & Kuncic, Z. (2003). Type II Solar Radio Bursts: Theory and Space Weather Implications. *Space Science Reviews*, 107(1), 27–34. doi: 10.1023/A:1025503201687
- Carbone, F., Sorriso-Valvo, L., Khotyaintsev, Y. V., Steinvall, K., Vecchio, A., Telloni, D., ... others (2021). Statistical Study of Electron Density Turbulence and Ion-cyclotron Waves in the Inner Heliosphere: Solar Orbiter Observations. *Astronomy & Astrophysics*, 656, A16. doi: 10.1051/0004-6361/202140931
- Chandran, B., Verscharen, D., Quataert, E., Kasper, J., Isenberg, P., & Bourouaine, S. (2013). Stochastic Heating, Differential Flow, and the Alpha-to-proton Temperature Ratio in the Solar Wind. *The Astrophysical Journal*, 776(1), 45. doi: 10.1088/0004-637X/776/1/45
- Chapman, S., Lee, R., & Dendy, R. (2005). Perpendicular Shock Reformation and Ion Acceleration. *Space Science Reviews*, 121(1), 5–19. doi: 10.1007/s11214-006-4481-x
- Chapman, S., & Zirin, H. (1957). Notes on the Solar Corona and the Terrestrial Ionosphere. *Smithsonian Contributions to Astrophysics*, 2(12). doi: 10.5479/si.00810231.2-1.1
- Colomban, L., Agapitov, O., Krasnoselskikh, V., Choi, K.-E., Kretzschmar, M., Dudok de Wit, T., ... others (2025). Polarization Properties of Whistler Waves from the First 17 Parker Solar Probe Encounters. *Geophysical Research Letters*, 52(10), e2025GL114622. doi: 10.1029/2025GL114622
- Colomban, L., Kretzschmar, M., Krasnoselkikh, V., Agapitov, O. V., Froment, C., Maksimovic, M., ... Bale, S. (2024). Quantifying the Diffusion of Suprathermal Electrons by Whistler Waves Between 0.2 and 1 AU with Solar Orbiter and Parker Solar Probe. *Astronomy & Astrophysics*, 684, A143. doi: 10.1051/0004-6361/202347489
- Dendy, R. O. (1995). *Plasma Physics: An Introductory Course*. Cambridge University Press.

- Dessler, A. J. (1967). Solar Wind and Interplanetary Magnetic Field. *Reviews of Geophysics*, 5(1), 1–41. doi: 10.1029/RG005i001p00001
- Dikpati, M., Suresh, A., & Burkepile, J. (2016). Cyclic Evolution of Coronal Fields from a Coupled Dynamo Potential-Field Source-Surface Model. *Solar Physics*, 291, 339–355. doi: 10.1007/s11207-015-0831-8
- Dmitriev, A., Crosby, N., & Chao, J.-K. (2005). Interplanetary Sources of Space Weather Disturbances in 1997 to 2000. *Space Weather*, 3(3). doi: 10.1029/2004SW000104
- Eddington, A. S. (1910). The Envelopes of Comet Morehouse (1908 c). *Monthly Notices of the Royal Astronomical Society*, 70(5), 442–458. doi: 10.1093/mnras/70.5.442
- Feldman, W., Asbridge, J., Bame, S., Montgomery, M., & Gary, S. (1975). Solar Wind Electrons. *Journal of Geophysical Research*, 80(31), 4181–4196. doi: 10.1029/JA080i031p04181
- Fisk, L. (1996). Motion of the Footpoints of Heliospheric Magnetic Field Lines at the Sun: Implications for Recurrent Energetic Particle Events at High Heliographic Latitudes. *Journal of Geophysical Research: Space Physics*, 101(A7), 15547–15553. doi: 10.1029/96JA01005
- Forslund, D. W. (1970). Instabilities Associated with Heat Conduction in the Solar Wind and their Consequences. *Journal of Geophysical Research*, 75, 17–28. doi: 10.1029/JA075i001p00017
- Galtier, S., & Buchlin, E. (2007). Multiscale Hall-magnetohydrodynamic Turbulence in the Solar Wind. *The Astrophysical Journal*, 656(1), 560. doi: 10.1086/510423
- Gary, S. P. (1978). Ion–acoustic–like Instabilities in the Solar Wind. *Journal of Geophysical Research: Space Physics*, 83, 2504–2510. doi: 10.1029/JA083iA06p02504
- Gary, S. P. (1993). *Theory of Space Plasma Microinstabilities* (No. 7). Cambridge university press.
- Gary, S. P., & Saito, S. (2007). Broadening of Solar Wind Strahl Pitch-angles by the Electron/electron Instability: Particle-in-cell Simulations. *Geophysical research letters*, 34(14). doi: 10.1029/2007GL030039
- Gary, S. P., Scime, E. E., Phillips, J. L., & Feldman, W. C. (1994). The Whistler Heat Flux Instability: Threshold Conditions in the Solar Wind. *Journal of Geophysical Research: Space Physics*, 99(A12), 23391–23399. doi: 10.1029/94JA02067
- Gedalin, M., Zhou, X., Russell, C. T., Drozdov, A., & Liu, T. Z. (2018). Ion Dynamics and the Shock Profile of a Low-Mach Number Shock. *Journal of Geophysical Research: Space Physics*, 123, 8913–8923. doi: 10.1029/2018JA025945
- Gingell, I., Schwartz, S. J., Burgess, D., Johlander, A., Russell, C. T., Burch, J. L., . . . others (2017). MMS Observations and Hybrid Simulations of Surface Ripples at a Marginally Quasi-parallel Shock. *Journal of Geophysical Research: Space Physics*, 122(11), 11–003. doi: 10.1002/2017JA024538
- Graham, D. B., & Cairns, I. H. (2013). Electrostatic Decay of Langmuir/Z-mode Waves in Type III Solar Radio Bursts. *Journal of Geophysical Research: Space Physics*, 118(7), 3968–3984. doi: 10.1002/jgra.50402
- Graham, D. B., & Cairns, I. H. (2014). Dynamical Evidence for Nonlinear Langmuir Wave Processes in Type III Solar Radio Bursts. *Journal of Geophysical Research:*

- Space Physics*, 119(4), 2430–2457. doi: 10.1002/2013JA019425
- Graham, D. B., & Khotyaintsev, Y. V. (2025). The Structure and Kinetic Ion Behavior of Low Mach Number Shocks. *Journal of Geophysical Research: Space Physics*, 130(5), e2024JA033283. doi: 10.1029/2024JA033283
- Graham, D. B., Khotyaintsev, Y. V., Dimmock, A. P., Lalti, A., Boldú, J. J., Tigik, S. F., & Fuselier, S. A. (2024). Ion Dynamics Across a Low Mach Number Bow Shock. *Journal of Geophysical Research: Space Physics*, 129. doi: 10.1029/2023JA032296
- Graham, D. B., Khotyaintsev, Y. V., Vaivads, A., Edberg, N. J. T., Eriksson, A. I., Johansson, E. P. G., . . . others (2021). Kinetic Electrostatic Waves and Their Association with Current Structures in the Solar Wind. *Astronomy & Astrophysics*, 656, A23. doi: 10.1051/0004-6361/202140943
- Grard, R. J. (1973). Properties of the Satellite Photoelectron Sheath Derived from Photoemission Laboratory Measurements. *Journal of Geophysical Research*, 78(16), 2885–2906. doi: 10.1029/JA078i016p02885
- Gringauz, K. I., Bezrokhikh, V. V., Ozerov, V. D., & Rybchinskii, R. E. (1960). A Study of the Interplanetary Ionized Gas, High-Energy Electrons and Corpuscular Radiation from the Sun by Means of the Three-Electrode Trap for Charged Particles on the Second Soviet Cosmic Rocket. *Soviet Physics Doklady*, 5, 361.
- Gurnett, D. A., & Anderson, R. R. (1977). Plasma Wave Electric Fields in the Solar Wind: Initial Results from Helios 1. *Journal of Geophysical Research*, 82, 632-650. doi: 10.1029/JA082i004p00632
- Gurnett, D. A., & Bhattacharjee, A. (2017). *Introduction to Plasma Physics: With Space, Laboratory and Astrophysical Applications* (Second Edition ed.). Cambridge University Press.
- Gurnett, D. A., & Frank, L. A. (1978). Ion Acoustic Waves in the Solar Wind. *Journal of Geophysical Research: Space Physics*, 83, 58-74. doi: 10.1029/JA083iA01p00058
- Halekas, J., Berčič, L., Whittlesey, P., Larson, D., Livi, R., Berthomier, M., . . . others (2021). The Sunward Electron Deficit: A Telltale Sign of the Sun's Electric Potential. *The Astrophysical Journal*, 916(1), 16. doi: 10.3847/1538-4357/ac096e
- Halekas, J., Whittlesey, P., Larson, D., Maksimovic, M., Livi, R., Berthomier, M., . . . others (2022). The Radial Evolution of the Solar Wind as Organized by Electron Distribution Parameters. *The Astrophysical Journal*, 936(1), 53. doi: 10.3847/1538-4357/ac85b8
- Halekas, J., Whittlesey, P., Larson, D., McGinnis, D., Maksimovic, M., Berthomier, M., . . . others (2020). Electrons in the Young Solar Wind: First Results from the Parker Solar Probe. *The Astrophysical Journal Supplement Series*, 246(2), 22. doi: 10.3847/1538-4365/ab4cec
- Hess, R. A., MacDowall, R. J., Goldstein, B., Neugebauer, M., & Forsyth, R. J. (1998). Ion Acoustic-like Waves Observed by Ulysses Near Interplanetary Shock Waves in the Three-dimensional Heliosphere. *Journal of Geophysical Research: Space Physics*, 103, 6531-6541. doi: 10.1029/97ja03395
- Hess, S., Malaspina, D., & Ergun, R. (2011). Size and Amplitude of Langmuir waves in the Solar Wind. *Journal of Geophysical Research: Space Physics*, 116(A7). doi: 10.1029/2010JA016163
- Horbury, T. S., O'Brien, H., Blazquez, I. C., Bendyk, M., Brown, P., Hudson, R., . . .

- Walsh, A. P. (2020). The Solar Orbiter Magnetometer. *Astronomy & Astrophysics*, 642, A9. doi: 10.1051/0004-6361/201937257
- Jagarlamudi, V., de Wit, T. D., Froment, C., Krasnoselskikh, V., Larosa, A., Berčić, L., ... others (2021). Whistler Wave Occurrence and the Interaction with Strahl Electrons During the First Encounter of Parker Solar Probe. *Astronomy & Astrophysics*, 650, A9. doi: 10.1051/0004-6361/202039808
- Jian, L., Russell, C., Luhmann, J., Anderson, B., Boardsen, S., Strangeway, R., ... Wennmacher, A. (2010). Observations of Ion Cyclotron Waves in the Solar Wind Near 0.3 AU. *Journal of Geophysical Research: Space Physics*, 115(A12). doi: 10.1029/2010JA015737
- Jian, L. K., Russell, C. T., Luhmann, J. G., Strangeway, R. J., Leisner, J. S., & Galvin, A. B. (2009). Ion Cyclotron Waves in the Solar Wind Observed by STEREO Near 1 AU. *The Astrophysical Journal*, 701(2), L105. doi: 10.1088/0004-637X/701/2/L105
- Johlander, A., Schwartz, S., Vaivads, A., Khotyaintsev, Y. V., Gingell, I., Peng, I., ... others (2016). Rippled Quasiperpendicular Shock Observed by the Magnetospheric Multiscale Spacecraft. *Physical Review Letters*, 117(16), 165101. doi: 10.1103/PhysRevLett.117.165101
- Kajdič, P., Blanco-Cano, X., Aguilar-Rodriguez, E., Russell, C. T., Jian, L. K., & Luhmann, J. G. (2012). Waves Upstream and Downstream of Interplanetary Shocks Driven by Coronal Mass Ejections. *Journal of Geophysical Research: Space Physics*, 117. doi: 10.1029/2011JA017381
- Karlsson, T., Heyner, D., Volwerk, M., Morooka, M., Plaschke, F., Goetz, C., & Hadid, L. (2021). Magnetic Holes in the Solar Wind and Magnetosheath Near Mercury. *Journal of Geophysical Research: Space Physics*, 126(5), e2020JA028961. doi: 10.1029/2020JA028961
- Kasper, J., Lazarus, A., & Gary, S. (2008). Hot Solar-wind Helium: Direct Evidence for Local Heating by Alfvén-cyclotron Dissipation. *Physical review letters*, 101(26), 261103. doi: 10.1103/PhysRevLett.101.261103
- Kellogg, P., Goetz, K., Monson, S., & Bale, S. (1999). Langmuir Waves in a Fluctuating Solar Wind. *Journal of Geophysical Research: Space Physics*, 104(A8), 17069–17078. doi: 10.1029/1999JA900163
- Kennel, C., Edmiston, J., & Hada, T. (1985). A Quarter Century of Collisionless Shock Research. *Geophysical Monograph Series*, 34, 1–36. doi: 10.1029/GM034p0001
- Khotyaintsev, Y. V., Graham, D. B., & Johlander, A. (2024). Ion Reflection by a Rippled Perpendicular Shock. *Physical Review Letters*, 133(21), 215201. doi: 10.1103/PhysRevLett.133.215201
- Khotyaintsev, Y. V., Graham, D. B., Vaivads, A., Steinvall, K., Edberg, N. J. T., Eriksson, A. I., ... Angelini, V. (2021). Density Fluctuations Associated with Turbulence and Waves. *Astronomy & Astrophysics*, 656, A19. doi: 10.1051/0004-6361/202140936
- Kilpua, E., Lumme, E., Andreeova, K., Isavnin, A., & Koskinen, H. (2015). Properties and Drivers of Fast Interplanetary Shocks Near the Orbit of the Earth (1995–2013). *Journal of Geophysical Research: Space Physics*, 120(6), 4112–4125. doi: 10.1002/2015JA021138
- Kretzschmar, M., Chust, T., Krasnoselskikh, V., Graham, D. B., Colombari, L.,

- Maksimovic, M., ... others (2021). Whistler Waves Observed by Solar Orbiter/RPW Between 0.5 AU and 1 AU. *Astronomy & Astrophysics*, 656, A24. doi: 10.1051/0004-6361/202140945
- Laakso, H., Pfaff, R., & Janhunen, P. (2002). Polar Observations of Electron Density Distribution in the Earth's Magnetosphere. 2. Density Profiles. *Annales Geophysicae*, 20(11), 1725–1735. doi: 10.5194/angeo-20-1711-2002
- Lalti, A., Khotyaintsev, Y. V., Graham, D. B., Vaivads, A., Steinvall, K., & Russell, C. T. (2022). Whistler Waves in the Foot of Quasi-perpendicular Supercritical Shocks. *Journal of Geophysical Research: Space Physics*, 127(5), e2021JA029969. doi: 10.1029/2021JA029969
- Lazar, M., López, R. A., Shaaban, S. M., Poedts, S., Yoon, P. H., & Fichtner, H. (2022). Temperature Anisotropy Instabilities Stimulated by the Solar Wind Suprathermal Populations. *Frontiers in Astronomy and Space Sciences*, 8, 777559. doi: 10.3389/fspas.2021.777559
- Lefebvre, B., Seki, Y., Schwartz, S. J., Mazelle, C., & Lucek, E. A. (2009). Reformation of an Oblique Shock Observed by Cluster. *Journal of Geophysical Research: Space Physics*, 114(A11). doi: 10.1029/2009JA014268
- Lemaire, J., & Scherer, M. (1971). Kinetic Models of the Solar Wind. *Journal of Geophysical Research*, 76(31), 7479–7490. doi: 10.1029/JA076i031p07479
- Lin, N., Kellogg, P. J., MacDowall, R., Tsurutani, B., & Ho, C. (1996). Langmuir Waves Associated with Discontinuities in the Solar wind: A Statistical Study. *Astronomy & Astrophysics*, v. 316, p. 425-429, 316, 425–429.
- Liu, J., Verscharen, D., Coburn, J., Nicolaou, G., Wu, X., Jiang, W., ... others (2025). Langmuir Wave Excitation in Solar-wind Magnetic Holes. *The Astrophysical Journal Letters*. doi: 10.3847/2041-8213/adea4f
- Lyons, L. (2003). Space plasma physics. In (p. 577-591). Elsevier. doi: 10.1016/B0-12-227410-5/00716-X
- Madanian, H., Halekas, J., Mazelle, C., Omid, N., Espley, J., Mitchell, D., & McFadden, J. (2020). Magnetic Holes Upstream of the Martian Bow Shock: MAVEN Observations. *Journal of Geophysical Research: Space Physics*, 125(1), e2019JA027198. doi: 10.1029/2019JA027198.1002/essoar.10501008.1
- Maksimovic, M., Bale, S. D., Chust, T., Khotyaintsev, Y., Krasnoselskikh, V., Kretschmar, M., ... Zouganelis, I. (2020). The Solar Orbiter Radio and Plasma Waves (RPW) Instrument. *Astronomy & Astrophysics*, 17, 20. doi: 10.1051/0004-6361/201936214
- Maksimovic, M., Pierrard, V., & Lemaire, J. (2001). On the Exospheric Approach for the Solar Wind Acceleration. *Astrophysics and Space Science*, 277(1), 181–187. doi: 10.1023/A:1012250027289
- Maksimovic, M., Zouganelis, I., Chaufray, J., Issautier, K., Scime, E. E., Littleton, J. E., ... Elliott, H. (2005). Radial Evolution of the Electron Distribution Functions in the Fast Solar Wind Between 0.3 and 1.5 AU. *Journal of Geophysical Research: Space Physics*, 110. doi: 10.1029/2005JA011119
- Mangeney, A., Grappin, R., & Velli, M. (1991). MHD Turbulence in the Solar Wind. In *Advances in Solar System Magnetohydrodynamics* (p. 327). Cambridge University Press New York.
- Marsch, E. (2006). Kinetic Physics of the Solar Corona and Solar Wind. *Living Reviews in Solar Physics*, 3. doi: 10.12942/lrsp-2006-1

- Marsch, E. (2018). Solar Wind and Kinetic Heliophysics. In *Annales geophysicae* (Vol. 36, pp. 1607–1630).
- Marsch, E., Mühlhäuser, K.-H., Schwenn, R., Rosenbauer, H., Pilipp, W., & Neubauer, F. (1982). Solar Wind Protons: Three-dimensional Velocity Distributions and Derived Plasma Parameters Measured Between 0.3 and 1 AU. *Journal of Geophysical Research: Space Physics*, *87*(A1), 52–72. doi: 10.1029/JA087iA01p00052
- Matteini, L., Landi, S., Hellinger, P., Pantellini, F., Maksimovic, M., Velli, M., . . . Marsch, E. (2007). Evolution of the Solar Wind Proton Temperature Anisotropy from 0.3 to 2.5 AU. *Geophysical Research Letters*, *34*, L20105. doi: 10.1029/2007GL030920
- McComas, D., Bame, S., Barraclough, B., Feldman, W., Funsten, H. O., Gosling, J., . . . others (1998). Ulysses' Return to the Slow Solar Wind. *Geophysical Research Letters*, *25*(1), 1–4. doi: 10.1029/97GL03444
- McComas, D., Elliott, H., Schwadron, N., Gosling, J., Skoug, R. M., & Goldstein, B. (2003). The Three-dimensional Solar Wind Around Solar Maximum. *Geophysical research letters*, *30*(10). doi: 10.1029/2003GL017136
- Mellott, M. (1985). Subcritical Collisionless Shock Waves. *Geophysical Monograph Series*, *35*, 131–140. doi: 10.1029/GM035p0131
- Melrose, D. (1980). The Emission Mechanisms for Solar Radio Bursts. *Space Science Reviews*, *26*(1), 3–38. doi: 10.1007/BF00212597
- Micera, A., Verscharen, D., Coburn, J. T., & Innocenti, M. E. (2025). Quasi-parallel Antisunward-propagating Whistler Waves Associated with the Electron Deficit in the Near-Sun Solar Wind: Particle-in-cell Simulation. *The Astrophysical Journal*, *979*(2), 226. doi: 10.3847/1538-4357/ada3d7
- Mott-Smith, H. M., & Langmuir, I. (1926). The Theory of Collectors in Gaseous Discharges. *Physical review*, *28*(4), 727. doi: 10.1103/PhysRev.28.727
- Mozer, F., Bale, S., Kellogg, P., Larson, D., Livi, R., & Romeo, O. (2022). An Improved Technique for Measuring Plasma Density to High Frequencies on the Parker Solar Probe. *The Astrophysical Journal*, *926*(2), 220. doi: 10.3847/1538-4357/ac4f42
- Müller, D., Cyr, O. C. S., Zouganelis, I., Gilbert, H. R., Marsden, R., Nieves-Chinchilla, T., . . . Williams, D. (2020). The Solar Orbiter Mission. *Astronomy & Astrophysics*, *642*, A1. doi: 10.1051/0004-6361/202038467
- Nakagawa, T., Ishii, T., Tsuruda, K., Hayakawa, H., & Mukai, T. (2000). Net Current Density of Photoelectrons Emitted from the Surface of the GEOTAIL Spacecraft. *Earth, planets and space*, *52*, 283–292. doi: 10.1186/BF03351637
- Neugebauer, M., & Snyder, C. W. (1962). Solar Plasma Experiment. *Science*, *138*, 1095-1097. doi: 10.1126/science.138.3545.1095.b
- Ofman, L., Balikhin, M., Russell, C. T., & Gedalin, M. (2009). Collisionless Relaxation of Ion Distributions Downstream of Laminar Quasi-perpendicular Shocks. *Journal of Geophysical Research: Space Physics*, *114*. doi: 10.1029/2009JA014365
- Ogilvie, K. W. (1975). Differences Between the Bulk Speeds of Hydrogen and Helium in the Solar Wind. *Journal of Geophysical Research*, *80*, 1335-1338. doi: 10.1029/JA080i010p01335
- Ogilvie, K. W., & Coplan, M. A. (1995). Solar Wind Composition. *Reviews of*

- Geophysics*, 33(S1), 615–622. doi: 10.1029/95RG00122
- Opher, M., Drake, J., Zieger, B., & Gombosi, T. (2015). Magnetized Jets Driven by the Sun: the Structure of the Heliosphere Revisited. *The Astrophysical Journal Letters*, 800(2), L28. doi: 10.1088/2041-8205/800/2/L28
- Opher, M., Loeb, A., Drake, J., & Toth, G. (2020). A Small and Round Heliosphere Suggested by Magnetohydrodynamic Modelling of Pick-up Ions. *Nature Astronomy*, 4(7), 675–683. doi: 10.1038/s41550-020-1036-0
- Owen, C. J., Abraham, J. B., Nicolaou, G., Verscharen, D., Louarn, P., & Horbury, T. S. (2022). Solar Orbiter SWA Observations of Electron Strahl Properties Inside 1 AU. *Universe*, 8(10), 509.
- Owen, C. J., Bruno, R., Livi, S., Louarn, P., Janabi, K. A., Allegrini, F., . . . Zouganelis, I. (2020). The Solar Orbiter Solar Wind Analyser (SWA) Suite. *Astronomy & Astrophysics*, 642, A16. doi: 10.1051/0004-6361/201937259
- Owens, M., Crooker, N., & Schwadron, N. (2008). Suprathermal Electron Evolution in a Parker Spiral Magnetic Field. *Journal of Geophysical Research: Space Physics*, 113(A11). doi: 10.1029/2008JA013294
- Parker, E. N. (1958). Dynamics of the Interplanetary Gas and Magnetic Fields. *Astrophysical Journal*, 128(7), 664. doi: 10.1038/nphys2664
- Parker, E. N. (2010). Kinetic and Hydrodynamic Representations of Coronal Expansion and The Solar Wind. In *Twelfth international solar wind conference* (Vol. 1216, p. 3-7). AIP. doi: 10.1063/1.3395887
- Pedersen, A., Lybekk, B., André, M., Eriksson, A., Masson, A., Mozer, F., . . . others (2008). Electron Density Estimations Derived from Spacecraft Potential Measurements on Cluster in Tenuous Plasma Regions. *Journal of Geophysical Research: Space Physics*, 113(A7). doi: 10.1029/2007JA012636
- Pierrard, V., Maksimovic, M., & Lemaire, J. (2001). Core, Halo and Strahl Electrons in the Solar Wind. *Astrophysics and Space Science*, 277(1), 195–200. doi: 10.1023/A:1012218600882
- Píša, D., Souček, J., Santolík, O., Hanzelka, M., Nicolaou, G., Maksimovic, M., . . . others (2021). First-year Ion-acoustic Wave Observations in the Solar Wind by the RPW/TDS Instrument on board Solar Orbiter. *Astronomy & Astrophysics*, 656, A14. doi: 10.1051/0004-6361/202140928
- Ramírez Vélez, J., Blanco-Cano, X., Aguilar-Rodriguez, E., Russell, C., Kajdič, P., Jian, L., & Luhmann, J. (2012). Whistler Waves Associated with Weak Interplanetary Shocks. *Journal of Geophysical Research: Space Physics*, 117(A11). doi: 10.1029/2012JA017573
- Reames, D. V. (2001). SEPs: Space Weather Hazard in Interplanetary Space. *Geophysical Monograph—American Geophysical Union*, 125, 101–108. doi: 10.1029/GM125p0101
- Reisenfeld, D. B., Gary, S., Gosling, J., Steinberg, J. T., McComas, D., Goldstein, B., & Neugebauer, M. (2001). Helium Energetics in the High-latitude Solar Wind: Ulysses Observations. *Journal of Geophysical Research: Space Physics*, 106(A4), 5693–5708. doi: 10.1029/2000JA000317
- Richard, L., Servidio, S., Svenningsson, I., Artemyev, A. V., Klein, K. G., Yordanova, E., . . . Khotyaintsev, Y. V. (2025). Non-Maxwellianity of Ion Velocity Distributions in the Earth’s Magnetosheath. *Physical Review E*, 112(5), L053201. doi: 10.1103/7p1x-84y9

- Rivera, Y. J., Badman, S. T., Stevens, M. L., Verniero, J. L., Stawarz, J. E., Shi, C., ... others (2024). In situ Observations of Large-amplitude Alfvén Waves Heating and Accelerating the Solar Wind. *Science*, 385(6712), 962–966. doi: 10.1126/science.adk6953
- Rodríguez-Pacheco, J., Wimmer-Schweingruber, R. F., Mason, G. M., Ho, G. C., Sánchez-Prieto, S., Prieto, M., ... Zong, Q. (2020). The Energetic Particle Detector. *Astronomy & Astrophysics*, 642, A7. doi: 10.1051/0004-6361/201935287
- Rosenbauer, H., Schwenn, R., Marsch, E., Meyer, B., Miggenrieder, H., Montgomery, M. D., ... Zink, S. M. (1977). A Survey on Initial Results of the HELIOS Plasma Experiment. *Journal of Geophysics Zeitschrift Geophysik*, 42(6), 561-580.
- Schroeder, J. M., Boldyrev, S., & Aulfalk, P. (2021). Stability of Superthermal Strahl Electrons in the Solar Wind. *Monthly Notices of the Royal Astronomical Society*, 507(1), 1329–1336. doi: 10.1093/mnras/stab2228
- Simnett, G. M. (2017). *Energetic Particles in the Heliosphere*. Springer.
- Souček, J., Píša, D., Kolmasova, I., Uhlir, L., Lan, R., Santolík, O., ... Bonnin, X. (2021). Solar Orbiter Radio and Plasma Waves - Time Domain Sampler: In-flight Performance and First Results. *Astronomy & Astrophysics*, 656. doi: 10.1051/0004-6361/202140948
- Stix, T. H. (1992). *Waves in Plasmas*. Springer Science & Business Media.
- Štverák, Š., Maksimovic, M., Trávníček, P. M., Marsch, E., Fazakerley, A. N., & Scime, E. E. (2009). Radial Evolution of Nonthermal Electron Populations in the Low-altitude Solar Wind: Helios, Cluster, and Ulysses Observations. *Journal of Geophysical Research: Space Physics*, 114(A5). doi: 10.1029/2008JA013883
- Štverák, Š., Trávníček, P., Maksimovic, M., Marsch, E., Fazakerley, A. N., & Scime, E. E. (2008). Electron Temperature Anisotropy Constraints in the Solar Wind. *Journal of Geophysical Research: Space Physics*, 113(A3). doi: 10.1029/2007JA012733
- Swanson, D. G. (2020). *Plasma Waves*. CRC Press.
- Tong, Y., Vasko, I. Y., Artemyev, A. V., Bale, S. D., & Mozer, F. S. (2019). Statistical Study of Whistler Waves in the Solar Wind at 1 au. *The Astrophysical Journal*, 878(1), 41. doi: 10.3847/1538-4357/ab1f05
- Treumann, R. A., & Baumjohann, W. (1997). *Advanced Space Plasma Physics* (First Edition ed.). Imperial College Press.
- Trotta, D., Dimmock, A., Hietala, H., Blanco-Cano, X., Horbury, T. S., Vainio, R., ... others (2025). An Overview of Solar Orbiter Observations of Interplanetary Shocks in Solar Cycle 25. *The Astrophysical Journal Supplement Series*, 277(1), 2. doi: 10.3847/1538-4365/ada4a7
- Tsurutani, B. T., Lakhina, G. S., Verkhoglyadova, O. P., Echer, E., Guarnieri, F. L., Narita, Y., & Constantinescu, D. O. (2011). Magnetosheath and Heliosheath Mirror Mode Structures, Interplanetary Magnetic Decreases, and Linear Magnetic Decreases: Differences and Distinguishing Features. *Journal of Geophysical Research: Space Physics*, 116(A2). doi: 10.1029/2010JA015913
- Tu, C.-Y., & Marsch, E. (1995). MHD Structures, Waves and Turbulence in the Solar Wind: Observations and Theories. *Space Science Reviews*, 73(1), 1–210. doi: 10.1007/BF00748891

- Turner, J., Burlaga, L., Ness, N., & Lemaire, J. (1977). Magnetic Holes in the Solar Wind. *Journal of Geophysical Research*, 82(13), 1921–1924. doi: 10.1029/JA082i013p01921
- Vasko, I., Krasnoselskikh, V., Tong, Y., Bale, S., Bonnell, J., & Mozer, F. (2019). Whistler Fan Instability Driven by Strahl Electrons in the Solar Wind. *The Astrophysical Journal Letters*, 871(2), L29. doi: 10.3847/2041-8213/ab01bd
- Verscharen, D., Chandran, B. D., Boella, E., Halekas, J., Innocenti, M. E., Jagarlamudi, V. K., ... others (2022). Electron-driven Instabilities in the Solar Wind. *Frontiers in Astronomy and Space Sciences*, 9, 951628. doi: 10.3389/fspas.2022.951628
- Verscharen, D., Chandran, B. D., Bourouaine, S., & Hollweg, J. V. (2015). Deceleration of Alpha Particles in the Solar Wind by Instabilities and the Rotational Force: Implications for Heating, Azimuthal Flow, and the Parker Spiral Magnetic Field. *The Astrophysical Journal*, 806(2), 157. doi: 10.1088/0004-637X/806/2/157
- Verscharen, D., Klein, K. G., & Maruca, B. A. (2019). *The Multi-scale Nature of the Solar Wind* (Vol. 16). Springer. doi: 10.1007/s41116-019-0021-0
- Volwerk, M., Goetz, C., Plaschke, F., Karlsson, T., Heyner, D., & Anderson, B. (2020). On the Magnetic Characteristics of Magnetic Holes in the Solar Wind Between Mercury and Venus. *Annales Geophysicae*, 38, 51-60. doi: 10.5194/angeo-38-51-2020
- Weber, E. J., & Davis Jr, L. (1967). The Angular Momentum of the Solar Wind. *Astrophysical Journal*, vol. 148, p. 217-227, 148, 217–227. doi: 10.1086/149138
- Wild, J., & Smerd, S. (1972). Radio Bursts from the Solar Corona. *Annual Review of Astronomy & Astrophysics*, 10, 159. doi: 10.1146/annurev.aa.10.090172.001111
- Wilkinson, W., Humphreys, M., & Kilgallon, S. (2023). The Link Between Individual Velocities in the Incident Plasma Flow and Ion Populations Upstream of Collisionless Shocks. *Journal of Geophysical Research: Space Physics*, 128(12), e2023JA031615. doi: 10.1029/2023JA031615
- Wilson III, L. (2016). Low Frequency Waves at and Upstream of Collisionless Shocks. *Geophysical Monograph Series*, 269–291. doi: 10.1002/9781119055006.ch16
- Wilson III, L., Cattell, C., Kellogg, P. J., Goetz, K., Kersten, K., Hanson, L., ... Kasper, J. C. (2007). Waves in Interplanetary Shocks: A Wind/WAVES Study. *Physical Review Letters*, 99. doi: 10.1103/PhysRevLett.99.041101
- Wilson III, L., Koval, A., Szabo, A., Stevens, M., Kasper, J., Cattell, C., & Krasnoselskikh, V. (2017). Revisiting the Structure of Low-Mach Number, Low-beta, Quasi-perpendicular Shocks. *Journal of Geophysical Research: Space Physics*, 122(9), 9115–9133. doi: 10.1002/2017JA024352
- Winterhalter, D., Neugebauer, M., Goldstein, B. E., Smith, E. J., Bame, S. J., & Balogh, A. (1994). Ulysses Field and Plasma Observations of Magnetic Holes in the Solar Wind and Their Relation to Mirror-mode Structures. *Journal of Geophysical Research: Space Physics*, 99, 23371-23381. doi: 10.1029/94JA01977.
- Wong, H., & Goldstein, M. (1988). Proton Beam Generation of Oblique Whistler Waves. *Journal of Geophysical Research: Space Physics*, 93(A5), 4110–4114. doi: 10.1029/JA093iA05p04110

Wu, C. S., Winske, D., Papadopoulos, K., Zhou, Y. M., Tsai, S. T., & Guo, S. C. (1983). A Kinetic Cross-field Streaming Instability. *Physics of Fluids*, *26*(5), 1259-1267. doi: 10.1063/1.864285

Zaslavsky, A., Romeo, O. M., Cherier, E., & Larson, D. E. (2025). Radial Evolution of the Strahl Pitch-angle Width. *Astronomy & Astrophysics*, *703*, A283. doi: 10.1051/0004-6361/202556524



# Acta Universitatis Upsaliensis

*Digital Comprehensive Summaries of Uppsala Dissertations from the Faculty of Science and Technology 2636*

Editor: The Dean of the Faculty of Science and Technology

A doctoral dissertation from the Faculty of Science and Technology, Uppsala University, is usually a summary of a number of papers. A few copies of the complete dissertation are kept at major Swedish research libraries, while the summary alone is distributed internationally through the series Digital Comprehensive Summaries of Uppsala Dissertations from the Faculty of Science and Technology. (Prior to January, 2005, the series was published under the title “Comprehensive Summaries of Uppsala Dissertations from the Faculty of Science and Technology”.)

Distribution: [publications.uu.se](http://publications.uu.se)  
urn:nbn:se:uu:diva-578455



ACTA UNIVERSITATIS  
UPSALIENSIS  
2026